CFD ANALYSIS OF AERODYNAMIC PERFORMANCE OF NACA 0018 AIRFOIL CONSIDERING SUCTION AND INTERNAL SLOT

by

Sumaiya Nawrin

MASTER OF SCIENCE IN MECHANICAL ENGINEERING

Department of Mechanical Engineering

BANGLADESH UNIVERSITY OF ENGINEERING AND TECHNOLOGY

DHAKA-1000, BANGLADESH

November, 2021

CFD ANALYSIS OF AERODYNAMIC PERFORMANCE OF NACA 0018 AIRFOIL CONSIDERING SUCTION AND INTERNAL SLOT

by

Sumaiya Nawrin

A Thesis Submitted to the Department of Mechanical Engineering, BUET
in Partial Fulfillment of the Requirements for the Degree of
MASTER OF SCIENCE IN MECHANICAL ENGINEERING

Supervised by

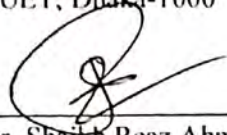**Dr. Mohammad Ali**
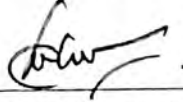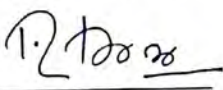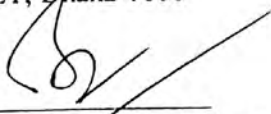Professor, Department of Mechanical Engineering

Department of Mechanical Engineering

BANGLADESH UNIVERSITY OF ENGINEERING AND TECHNOLOGY

DHAKA-1000, BANGLADESH

November, 2021

II

The thesis titled **"CFD Analysis of Aerodynamic Performance of NACA 0018 Airfoil Considering Suction and Internal Slot"** submitted by Sumaiya Nawrin, Roll: 1015102011, Session: October-2015 has been accepted as satisfactory in partial fulfillment of the requirements for the degree of Master of Science in Mechanical Engineering on 30 November, 2021.

BOARD OF EXAMINERS

1.

Dr. Mohammad Ali
Professor
Department of Mechanical Engineering
BUET, Dhaka-1000

Chairman
(Supervisor)

2.

Dr. Shaikh Reaz Ahmed
Professor & Head
Department of Mechanical Engineering
BUET, Dhaka-1000

Member
(Ex- officio)

3.

Dr. Mohammad Mamun
Professor
Department of Mechanical Engineering
BUET, Dhaka-1000

Member

4.

Dr. A.B.M. Toufique Hasan
Professor
Department of Mechanical Engineering
BUET, Dhaka-1000

Member

5.

Dr. A. K. M. Sadrul Islam
Ex. Professor
Department of Mechanical Engg., BUET,
Apt# A4, House# 110, Road# 9/A,
Dhanmondi, Dhaka-1209, Bangladesh

Member
(External)

DECLARATION

This is to certify that this thesis titled "CFD Analysis of Aerodynamic Performance of NACA 0018 Airfoil Considering Suction and Internal Slot" is carried out by the author Sumaiya Nawrin under the supervision of Dr. Mohammad Ali, Professor, Department of Mechanical Engineering, BUET.

It is hereby declared that this thesis or any part of it has not been submitted elsewhere for the award of any degree or diploma.

Sumaiya Nawrin

Sumaiya Nawrin
Roll No: 1015102011

Dedicated

to

My Beloved Parents

ACKNOWLEDGEMENT

ABSTRACT

The control of flow separation is one of the important ways for the reduction of drag as well as the increase of lift to drag ratio. In the domain of aerospace technology the main focus of this study is the enhancement of lift force, the reduction of drag force and in combination the enhancement of lift to drag ratio. In order to achieve these objectives, both active and passive controls of flow separation on 2D NACA 0018 airfoil are considered and CFD simulation is performed on this configuration. The computational runs are made at Reynolds number 7.12×10^6 and angles of attack ranges from $0° \sim 25°$. This investigation primarily focuses on the flow separation delay by suction with a slot of width 2% of the chord length placed at different locations of the airfoil to find optimum position. Suction pressures are expressed as the percentage of atmospheric pressure and accordingly four different suction pressures: 44%, 54%, 64% and 74% are considered to find out the best suction position based on the aerodynamic performances.

As a passive flow control of separation, two different configurations of internal slots are then introduced, one is tangential internal slot and the other is leading edge chordal slot. The result shows that the performance of tangential internal slot is better in comparison to that of leading edge chordal slot. For getting better result, the optimum position of tangential internal slot is sought and considered for further CFD simulation and analysis of the result.

Finally, the combined effects of tangential internal slot near the leading edge and suction near the trailing edge are studied. The result shows that the combination of suction and tangential internal slot moves the separation point from 46% to 72% of the chord length while for only tangential internal slot the separation occurs at 68% of the chord length. The detached flow reattaches at 97% of the chord length position for plain airfoil with and without the tangential internal slot and for the combined effect of suction and tangential internal slot the reattachment occurs at 73% of the chord length position. This modified configuration increases lift force, decreases drag force and increases lift to drag ratio significantly. The tangential internal slot increases lift to drag ratio as 9% compared with plain airfoil whereas the combination of tangential internal slot and suction increases 17% lift to drag ratio. The result also shows that the stall angle is increased by this modified configuration in airfoil. The outcome of this investigation might help the airfoil designers to achieve much better aerodynamic performance.

CONTENTS

x

XIII

AOA	Angle of Attack
C	Chord
C_D	Drag Coefficient
CFD	Computational Fluid Dynamics
CG	Center of Gravity
C_L	Lift Coefficient
CL	Center of Lift
C_O	Root Chord
C_T	Tip Chord
D	Drag Force
FVM	Finite Volume Method
L	Lift Force
P	Pressure
P_∞	Free Stream Static Pressure
R_e	Reynolds Number
V_∞	Free Stream Fluid Velocity
∇	Del Operator
ρ	Density
ρ_∞	Free Stream Fluid Density

INTRODUCTION

1.1 General

Mankind has always a wish to fly like birds, even for such a brief moment. The Wright Brothers [1] were the first to give a ray of hope in this aspect. From then, there is a lot of progression in the history of aviation industry and it is predominantly focused to escalate the maneuverability of the aircraft. In the domain of aerospace technology, flow separation is the foremost obstacle which is correlated with the wings of an aircraft. In order to elevate aerodynamic efficiency, flow separation control is much needed aspect.

Most of the drag augmentations are closely integrated with the wing during flying condition. Flow separation can also be the reason of vortex shedding, which can generate unwanted vibrations and instability. Undesirable drag forces can have a huge effect on the fuel consumption of an aircraft. And that is the reason why engineers go to great lengths to design aircraft wing accurately. Efficient design plays an indispensable role to enhance wing performance as well as to have a fuel efficient, smooth and safe flight.

1.2 Literature Review

An efficient wing configuration design can delay the occurrence of flow separation. In aerodynamics, wings are the key aerodynamic structure of an aircraft which make it possible for the aircraft to fly. The accessible literatures emphasizes on the techniques applied on airfoil in order to achieve expected augmentation of lift to drag ratio as well as flow separation delay by varying the airfoil structure. The available literatures related with the present study are discussed below:

There were numerous literatures that focused on active flow control mechanism to observe flow separation delay. Huang et al. [2] conducted a numerical study of blowing and suction control mechanism on NACA 0012 airfoil at a Reynolds number of 5×10^5 and an angle of $18°$. From a mechanism perspective, suction took the advantage of creating a larger and lower

pressure, Cp zone on the airfoil's upper surface to increase lift and eventually the flow got more attached. Vrchota et al. [3] tested several actuators locations and active flow control strategies with computational fluid dynamics. The separation onset had been postponed by about 2° of angle of attack; the value of lift-to-drag (L/D) was improved up to 22 per cent for the most beneficial cases. Zalovick [4] studied an investigation of the effectiveness of suction slots as a means of extending the laminar boundary layer had been made in flight at high Reynolds numbers on an NACA 35-215 airfoil. The results had shown that with nine slots spaced about 5 percent of the chord the laminar boundary layer on the upper surface could be maintained, by withdrawing air from the boundary layer, to or slightly beyond 45 percent or just about the minimum pressure point, over a range of airplane lift coefficient from 0.19 to about 0.35.

Müller-Vahl et al. [5] experimentally explored the utility of constant blowing as an aerodynamic load control concept for wind turbine blades. Blowing from the leading-edge slot showed a significant potential for load control applications. The effects of steady slot suction as a means of controlling separation on a blunt elliptical airfoil were investigated and compared to the effects of steady blowing applied to the same airfoil previously investigated by Chen et al. [6]. Slots whose width approached 1% of the chord was located downstream of the natural separation location and generated the highest lift for a given dimensionless mass-flow coefficient. Radespiel et al [7] reviewed progress in active flow control by steady blowing. It appeared that two strategies of blowing deserve particular attention. The sensitivities of these two approaches as observed in fundamental flow investigations and in applications were described and analyzed as suited efficiency parameters of blowing.

Yousefi et al. [8] evaluated the effects of jet width on blowing and suction flow control evaluated for a NACA 0012 airfoil. Results of this study demonstrated that when the blowing jet width increases, the lift-to-drag ratio rises continuously in tangential blowing and decreases quasi-linearly in perpendicular blowing. Zhu et al. [9] presented the review of jet flow control techniques which had been used or were worth being used in VAWTs, including the blowing, synthetic and plasma jet actuators. However, the jet flow control strategies to reduce the energy or matter consumption of jet actuators for VAWTs should be developed. The results showed that the upward-parabola blowing control strategy could dramatically enhance the aerodynamic performance by using significantly low energy or matter consumption. Liu et al. [10] developed a new suction-blowing joint control technique to

reduce airfoil drag. The numerical results showed that suction-blowing control results in a lower drag compared with suction without blowing. Narsipur et al. [11] studied the variation of leading-edge suction slot using computational results for steady and unsteady airfoil motions. Results show that flow field structures of unsteady low pitch rate motions are similar to steady results for a given amount of trailing-edge separation. Ibrahim et al. [12] did both experimental and computational investigation on the effect of slot cavities on a supersonic projectile. A single configuration of the slot pattern was used with two different slot widths (0·5mm and 2·0mm). It was found that the reduction in total drag was modest when the width was 0·5mm.

Anuraj et al. [13] investigated to identify the optimum location for suction which provided maximum lift augmentation. The critical Reynolds number occurred at around 95% of the length instead of 45% of the length when the same experiment was conducted without suction. Azim et al. [14] numerically investigated the aerodynamic performance for the delay of boundary layer separation by suction in NACA 4412 airfoil surface. The result showed that the lift to drag ratio during suction was approximately 2.24 times higher than that of without suction. Zhang et al. [15] investigated the effects using high lift zero-net mass-flux Co-Flow Jet (CFJ) active flow control airfoil with plain flaps and with no flap. The 2D numerical studies indicated that a plain flap could dramatically increase the lift coefficient and aerodynamic efficiency simultaneously compared with the conventional control surface with the same size of flap and deflection angle. Petz et al [16] described experimental results of controlling flow separation by periodic excitation on the flap of a generic high-lift configuration. By preventing the flow from separating or by reattaching the separated flow, lift and drag were substantially improved, resulting in a lift-to-drag ratio enhancement of 20–25%.

Previous studies also emphasized on passive flow control mechanism regarding flow separation control. Gardarin et al. [17] conducted experimental investigation of flow separation control for an internal flow backward-facing ramp. An embedded rectangular vane VG was used, and they suggested that the VG should be placed before the occurrence of the separation line. Serakawi et al. [18] described an experimental study of the effects of passive half-delta wing vortex generators on a backward-facing ramp flow. The results showed that an array of vortex generators with an aspect ratio of 1.6 had the highest efficiency in reducing the flow separation region. Seshagiri et al. [19] presented a low-speed wind-tunnel

investigation in detailing the effects of vortex generators on an airfoil at low Reynolds numbers. The data suggested that the static vortex generators function similarly to those at higher Reynolds numbers; increasing the maximum lift coefficient and increasing the stall angle. Luo et al. [20] investigated the effect of passive flow control using a microcylinder near the leading edge of a stalled airfoil (NACA 0012) at a Reynolds number of 6×10^6 through a computational study. Johari et al. [21] measured lift, drag, and pitching moments of airfoils with leading-edge sinusoidal protuberances in a water tunnel and compared with those of a baseline 634-021 airfoil. The amplitude of the protuberances had a distinct effect on the performance of the airfoils, whereas the wavelength had little. Flow visualization indicated separated flow originating primarily from the troughs and attached flow on the peaks of the protuberances at angles beyond the stall angle of the baseline foil.

Numerical investigations and design optimization had been performed by Joo et al. [22] to demonstrate the benefits of a combined nose droop and Gurney flap for improving dynamic stall and post stall aerodynamic characteristics of a rotor airfoil. It indicates that by the deliberate combination of a Gurney flap and nose droop, enhancement of lift and pitching moment characteristics in dynamic stall can be achieved. Lawson et al. [23] aimed to assess changes of the cavity geometry and their effect on the resulting flow using detached-eddy simulation. All of the devices tested achieved similar reductions in overall sound pressure level in the rear half of the cavity; however, a slanted aft wall provided the largest noise reduction in the front half of the cavity. Chauhan et al. [24] experimentally investigated flow control over a square cylinder using an attached splitter plate. The experiments are mainly conducted at a Reynolds number of 485. A correlation is found between the splitter plate length, Reynolds number, and the drag coefficient. Kolzsch et al. [25] presented experimental results of vortex-flow manipulation on a generic delta-wing configuration using pulsed blowing slot actuators along the leading edge.

Obiga [26] executed wind tunnel and numerical investigation of the effect of a unique slot configuration and its geometric parameters on the aerodynamic performance of a NACA0018 airfoil at low Reynolds number. Comparing the slotted and plain airfoils, the aerodynamic force data showed that the presence of the slots was detrimental to aerodynamic performance especially when the slot location is closer to the leading edge. Therefore, a 2D numerical parametric study of slot width and slope was carried out using ANSYS FLUENT 16.0 with the intention of improving the lift–to–drag (L/D) ratio of the span–length slotted airfoils.

4

Moshfeghi et al. [27] numerically investigated effects of a passive flow control method on aerodynamic performance horizontal axis wind turbine by splitting its blades along the span. From the point of view of an appropriate design, the results demonstrated that a well-designed split location should meet several criteria such as: the location of split on the pressure surface which needed to be near to stagnation point, the split location at the suction surface which should be deep inside the separated area, and also the inject flow angle which had to be tangent to the blade suction surface. Belamadi et al [28] explored the improvement of aerodynamic characteristics of wind turbine airfoils under stall conditions through passive boundary layer control using slots. An extensive 2D-numerical study had been done to analyze the effects of slot location, width and slope and the best configuration was determined. Simulations were done using steady RANS equations; the turbulence closure model had been chosen among four possible choices (standard k–ε, Spalart–Allmaras, k–ω and k–ω SST) based on comparison with experimental results. The results showed that the control system improves aerodynamic performance only over a specific range of angles of attack.

Ni et al. [29] discussed application of a custom optimized-design internal slot on a NACA 634-021 airfoil blade to allow ventilation of flow through the slot from the pressure side to the suction side of the blade, in support of delaying flow separation and stall where the flow details obtained from the CFD study provided better insight into the underlying control mechanism of the internal slot. Ni et al. [30] also studied the combined effect of an internal slot in an airfoil and transverse leading-edge tubercles on its performance. It was shown that the slot resulted in further improvement of the post- stall performance.

1.3 Motivation of the Present Research Work

As per literature review, researchers from all over the world have been carried out numerous experimental and numerical investigations in order to achieve expected augmentation of lift to drag ratio by varying the airfoil structure. Previous studies have shown that slot position with suction pressure is a feasible approach to delay flow separation. The present research focuses on the individual and combined effects of suction and internal slot on the upper surface of airfoil. These modified features act as a combination of active and passive flow

5

control mechanism to observe the better aerodynamic performance by computational fluid dynamics.

1.4   Problem Statement

Airfoil is the core part of an aircraft and the physics behind this simple shape is revolutionizing the aerodynamics technology. Wind turbines, gas turbines, hydraulic turbines, hydraulic machines and many others work on the principles of airfoil. During flight, airfoil technology has a massive impact on the cruise speed, stall speed, take-off and landing phenomenon. While aircraft is in flight there are four forces acting upon it. They are lift, weight, thrust and drag. Lift is the upward force created by the wings as air flows around them and keeps the airplane in the air. Weight is the downward force toward the center of the earth opposite lift which exists due to gravity. Thrust is the forward force generally created by the aircraft's propellers or turbine engines which pulls or pushes the aircraft through the air. Drag is the force acting in the direction opposite of thrust which fundamentally limits the performance of the airplane.

In normal flight as air flows around the wing, the air deflects downward as it flows around it and as a result the wind will lift the wing up. Typically the drag force increases with the increment of lift force. Hence, the overall aerodynamic efficiency cannot improve entirely and ultimately leads to flow separation. So, the researchers are always making an effort to find out the increased lift and decreased drag phenomenon on differently shaped airfoil structure. The present study may guide the aircraft designers to pick out a better airfoil shape to increase the overall lift to drag ratio for fuel-efficient flying.

1.5   Scope and Objectives of the Research

The proposed numerical investigation is carried out to witness individual and combined effects of internal and suction slot with suction pressure on airfoil. Comparison of plain and modified airfoil with different angles of attack will be performed to get highest lift and lowest drag by flow separation delay.

However, the objectives with specific aims are as follows:

i.   To investigate the performance of airfoil at different slot locations with suction pressure on upper surface at various angles of attack.

ii. To compare the effect of two different configuration of internal slot on airfoil at various angles of attack.

iii. To analyze the combined effects of internal slot and suction slot with suction pressure on the upper surface of airfoil in order to observe the aerodynamic performance.

iv. To identify the optimum parameter among all the considered parameters for the better performance of airfoil.

1.6   Organization of the Thesis

The assessment is divided into six chapters as follows:

i.   The first chapter focuses on the background information associated with the literature review, motivation, problem statement, scope and objectives of the present investigation.

ii. The second chapter reviews on the overview of the wing aerodynamics.

iii. The third chapter illustrates the computational method of the current research work.

iv. The fourth chapter describes the numerical results and discussion on the fundamental aspects of the results.

v.   Finally, the fifth chapter concludes the comprehensive research and also suggests few scopes for upcoming research in the near future in comparison with the current study.

OVERVIEW OF WING AERODYNAMICS

2.1 Wing and Airfoil

The wing is the fundamental aerodynamic structure that generates lift while moving through air. The plan form of a wing is the shape of a wing seen on a plan view of the aircraft [31]. Basically, wing is a three dimensional component while airfoil is two dimensional component. An airfoil is the cross sectional shape of a wing which is designed to manipulate the flow of air to produce lift. The ideal shape of airfoil depends on how fast and what altitude it is going to be flown at but they all are shaped to manipulate the flow of air to generate a force.
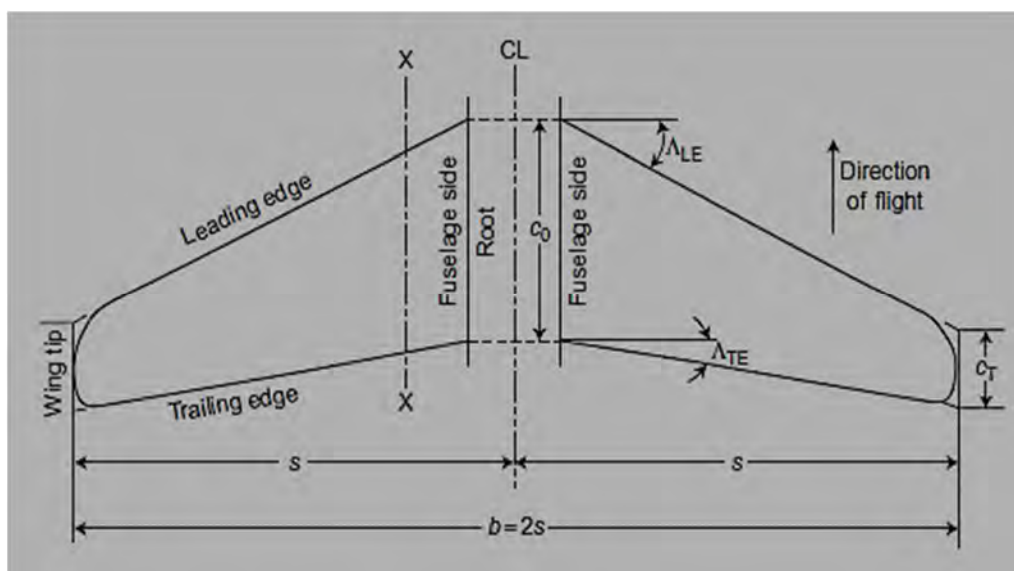
Figure 2.1: Wing plan form geometry [31]

If a horizontal wing is cut by a vertical plane parallel to the center-line, such as X-X in Figure 2.1, the shape of the resulting section is usually of a type shown in Figure 2.2 (c). In a cambered/ asymmetric airfoil, chord line is just an imaginary line that gets drawn from the trailing edge through the leading edge. At any distance along the chord from the nose, a point may be marked mid-way between the upper and lower surfaces. The locus of all such points, usually curved, is the median line of the section, usually called the camber line. The camber

is basically the shape or the curvature of the airfoil. A symmetric airfoil shown in Figure 2.2 (a) has same shape on both sides of the centerline. For a symmetric airfoil, mean camber line is the line that is halfway between the upper and lower surface of the airfoil. Hence, the mean camber line and chord line of a symmetric airfoil will be the same.
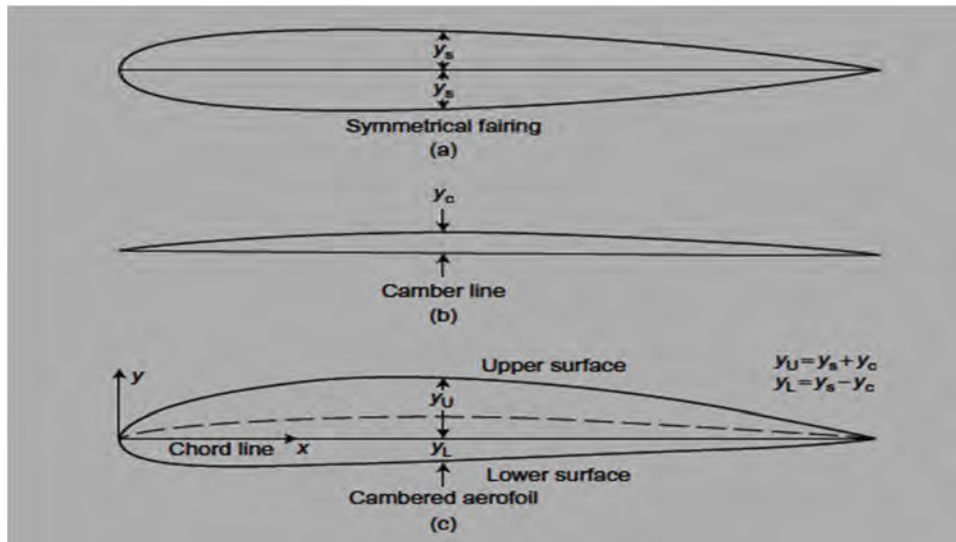
Figure 2.2: Airfoil section geometry [31]

2.2   Aerodynamic Forces Developed by Airfoil

Airplanes move in three dimensions. They move around the lateral axis that extends from wingtip to wingtip, the vertical axis that extends up to the middle, and then the longitudinal axis that extends from the nose through the tail. Thrust, drag, lift, and weight are forces that act upon all aircraft in flight. Understanding how these forces work and knowing how to control them with the use of power and flight controls are essential to flight. This section [31] discusses the aerodynamics of flight—how design, weight, load factors, and gravity affect an aircraft during flight maneuvers. The four forces acting on an aircraft are defined as follows:

- Thrust—the forward force produced by the power plant/ propeller or rotor. It opposes or overcomes the force of drag. As a general rule, it acts parallel to the longitudinal axis.

9

- Drag—a rearward, retarding force caused by disruption of airflow by the wing, rotor, fuselage, and other protruding objects. As a general rule, drag opposes thrust and acts rearward parallel to the relative wind.

- Lift—is a force that is produced by the dynamic effect of the air acting on the airfoil, and acts perpendicular to the flight path through the center of lift (CL) and perpendicular to the lateral axis. In level flight, lift opposes the downward force of weight.

- Weight—the combined load of the aircraft itself, the crew, the fuel, and the cargo or baggage. Weight is a force that pulls the aircraft downward because of the force of gravity. It opposes lift and acts vertically downward through the aircraft's center of gravity (CG).

In steady flight, the sum of these opposing forces is always zero. There can be no unbalanced forces in steady, straight flight based upon Newton's Third Law, which states that for every action or force there is an equal, but opposite, reaction or force. This is true whether flying level or when climbing or descending.
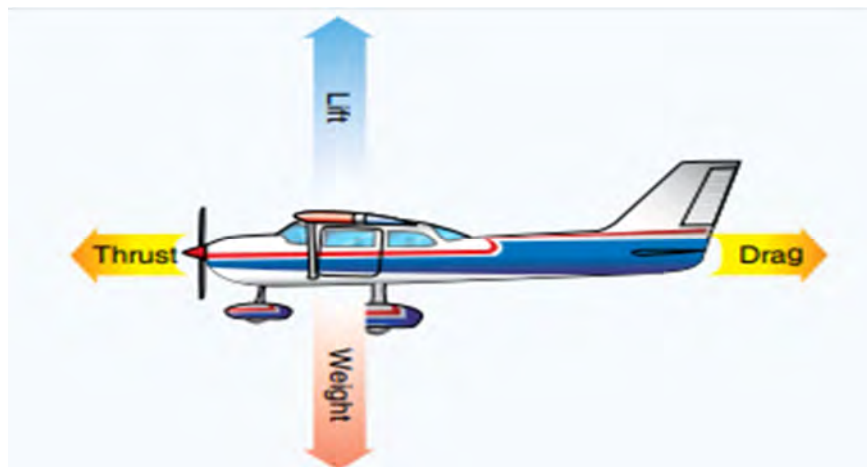
Figure 2.3: Forces acting on an aircraft [32]

It does not mean the four forces are equal. It means the opposing forces are equal to, and thereby cancel, the effects of each other. In Figure 2.3, the force vectors of thrust, drag, lift, and weight appear to be equal in value. Another important concept is angle of attack (AOA). Since the early days of flight, AOA is fundamental to understanding many aspects of airplane

performance, stability and control. The AOA is defined as the acute angle between the chord line of the airfoil and the direction of the relative wind as shown in Figure 2.4:

Figure 2.4: Angle of attack during flight

The measurement of the pressure distribution [33] is often carried out during flight testing on new aircraft designs and during flight research programs. The importance of the measurement lies with the ability to verify numerical predictions of the pressure distribution and/or any scale wind tunnel testing that has been carried out. The measurement of the air pressure distribution also enables flight loads to be calculated and this provides a verification that the aircraft structure is operating within the design loading conditions.

This work is focused on the lift force that is generated by distributions in air pressure. During steady-state flight, the weight force of an aircraft will be balanced by the lift generated, while for a powered aircraft the drag of the aircraft will be balanced by the thrust produced. The forces acting on an aircraft due to air can be divided into pressure forces and shear forces shown in Figure 2.5.
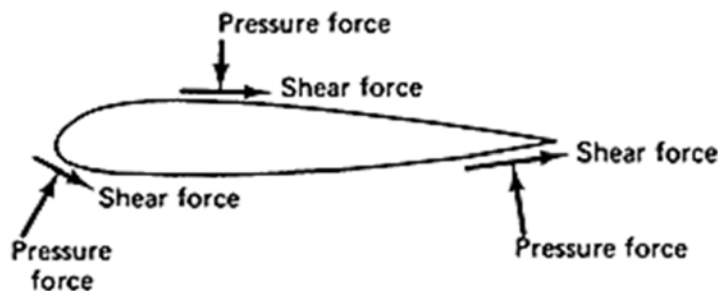
Figure 2.5: Total forces acting on an airfoil section can be broken into pressure and shear forces. [33]

Shear forces are due to the viscosity of the air while pressure forces are created by changes in air velocity as it passes over the aircraft. The distribution of pressure over an airfoil creates a

net resultant force that is typically broken up into components; lift and drag forces relative to the free stream direction or normal and axial forces relative to the airfoil. The resultant force is usually expressed as a lift force, drag force and a moment acting about a point located at a quarter of the total chord length from the leading edge of the airfoil.
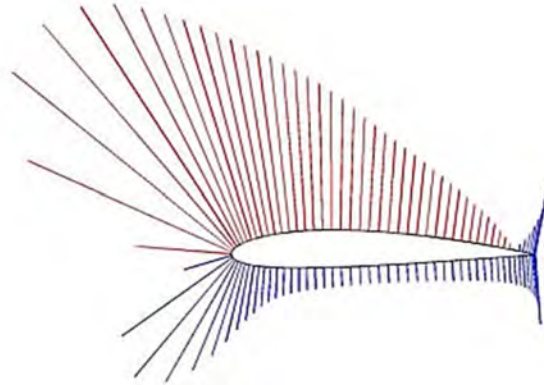
Figure 2.6: Typical distribution of pressure over an airfoil. Red lines represent pressures lower than atmospheric while blue lines represent pressures higher than atmospheric. [33]

Figure 2.6 shows a typical pressure distribution over an airfoil. The pressures acting on an airfoil at any point are non-dimensionalised into pressure coefficients according to equation 2.1.

$$C_p = \frac{p - p_\infty}{\frac{1}{2}\rho_\infty v_\infty^2}$$
(2.1)

where, p is the pressure at any point on the surface;

p_∞ is the free stream static pressure ;

v_∞ is the free stream fluid velocity;

ρ_∞ is the free stream fluid density.

2.3   Aerodynamic Drag

When fluid flows past an object, or an object moves through a stationary fluid, the fluid exerts a force on the object. This force can be split into two components. One of them acting in the same direction as the fluid flows is called drag. So, drag is the force experienced by an object representing the resistance to its movement through a fluid. Sometimes called wind resistance or fluid resistance, it acts in the opposite direction to the relative motion between the object and the fluid. The example opposite shows the aerodynamic drag forces

12

experienced by an airfoil or aircraft wing moving through the air with constant angle of attack as the air speed is increased.

The Total Aerodynamic Drag is the sum of the following components:

Induced Drag – It occurs due to the vortices and turbulence resulting from the turning of the air flow and the downwash associated with the generation of lift. It Increases with the angle of attack and is inversely proportional to the square of the air speed.

Form Drag or Pressure Drag – It occurs due to the size and shape of the airfoil and it increases with the square of air speed. Streamlined shapes are designed to reduce form drag.

Friction Drag – It arises from the friction of the air against the "skin" of the airfoil moving through it. It increases with the surface area of the airfoil and the square of air speed.

Profile Drag or Viscous Drag- It is the sum of Friction Drag and the Form Drag.

Parasitic Drag or Interference Drag – It is incurred by the non-lifting parts of the aircraft such as the wheels, fuselage, tail fins, engines, handles and rivets. It increases with the square of air speed. Parasitic drag becomes dominant at higher air speeds.

Wave Drag – It occurs due to the presence of shock waves occurring on the blade tips of aircraft and projectiles. Associated with passing the sound barrier it is a sudden and dramatic increase in drag which only comes into play as the vehicle increases speed through transonic and supersonic speeds.
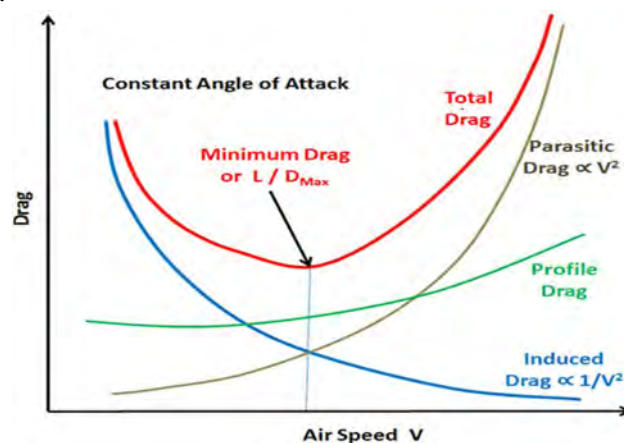
Figure 2.7: Components of drag

Figure 2.7 shows different components of drag force. Most of the time these drag forces are undesirable. They can have a huge effect on the fuel consumption and performance of air vehicles. And so engineers go to great lengths to minimize them.

2.4 Drag Coefficient (C_D)

Drag coefficient is also called fluid dynamic drag. It is the resistance of an object when it moves through a fluid. It is a dimensionless quantity and allows aerodynamicists to account for the influence of shape, inclination and flow conditions when calculating aerodynamic drag. The following equation represents the drag coefficient.

$$C_D = \frac{D}{\frac{1}{2}\rho v^2 C} \tag{2.3}$$

where, D= Drag force

2.5 Aerodynamic Lift

Lift is the force that directly opposes the weight of an airplane and holds the airplane in the air. Lift is generated by every part of the airplane, but most of the lift on a normal airliner is generated by the wings. Lift is a mechanical aerodynamic force produced by the motion of the airplane through the air. Because lift is a force, it is a vector quantity, having both a magnitude and a direction associated with it. Lift acts through the center of pressure of the object and is directed perpendicular to the flow direction. There are several factors which affect the magnitude of lift. Lift producing airfoils can obviously be found in airplane wings, but also in many other applications like wind turbine blades or propeller blades.

As the fluid flows around the airfoil, it creates two different types of stress which act on its surface. The wall shear stresses act tangential to the object's surface and are cause by the frictional forces that act on the airfoil because of the fluid's viscosity. The pressures stresses act perpendicular to the object's surface and are caused how pressure is distributed around it. Lift is the resultant of these two stresses in the direction perpendicular to the flow. The only way the fluid can impart a force onto an object is through these stresses. Integrating the stresses in the lift direction over the surface of the airfoil gives the lift force. For streamlined bodies like airfoils, the shear stresses will mostly be acting in the same direction as the flow.

14

They will make a large contribution to the drag force, but won't contribute a significant amount to the lift force. And so we can neglect them and say that the lift acting on an airfoil is caused by the way pressure is distributed around it.

2.6   Lift Coefficient (C_L)

Coefficient of lift uses the symbol C_L to measure the lift of an airfoil section or a wing as the angle of attack of the airfoil or wing changes the coefficient of lift. So, the lift coefficient is a number that aerodynamicists use to model all of the complex dependencies of shape, inclination, and some flow conditions on lift. The equation can be written as below:

$$C_L = \frac{L}{\frac{1}{2}\rho v^2 C}$$

(2.2)

where, L= Lift force

2.7   Theory on Flow Separation

During flow separation on a surface, the velocity boundary layer gets detached from it and leads to an unsteady flow conditions. From drag forces it is known that pressure drag is essentially caused by a pressure difference between the front and rear of an object. Pressure drag increases significantly if flow separation occurs and it happens when the fluid boundary layer detaches from the body, creating a wake of recirculating flow.
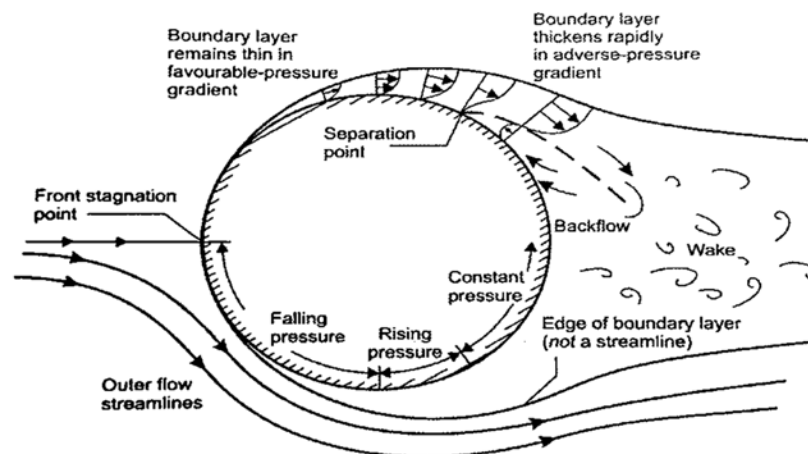
Figure 2.8: Boundary layer separation over a cylinder [34]

15

This creates an area of separation region and results in a large drag force. To reduce drag force, we have to minimize flow separation at all costs. Flow separation can also cause vortex shedding, which can generate unwanted vibrations and instability.

In Figure 2.8 as the fluid passes over the surface of the sphere it is initially accelerating, and so pressure is decreasing in the direction of the flow. This is called a favorable pressure gradient. Beyond a certain point the flow then begins to decelerate, and so pressure in the flow is increasing. This increase in pressure is called the adverse pressure gradient, and it has a significant effect on the flow close to wall.
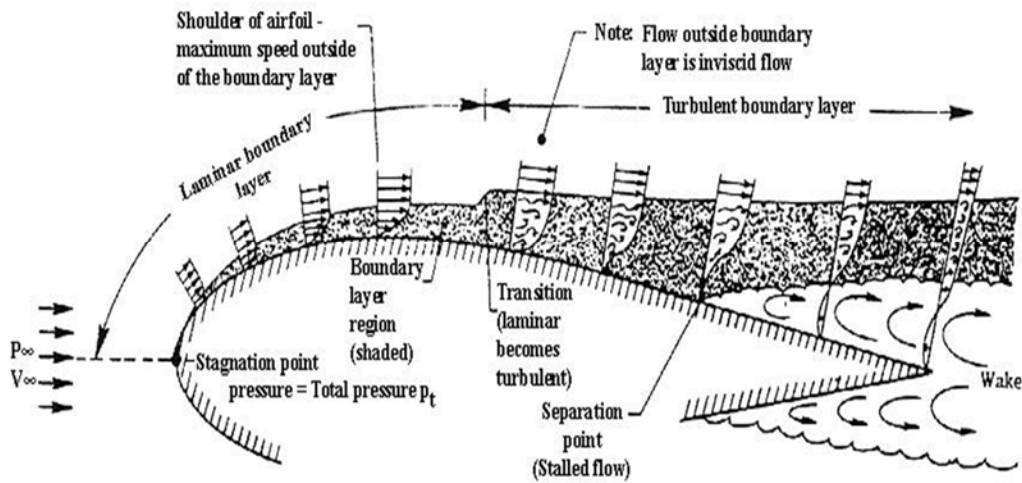
Figure 2.9: Boundary layer separation over the top of a wing [34]

If the increase of pressure is large, the flow will reverse direction and since it can't travel backwards because of the oncoming fluid it detaches from the surface, resulting in flow separation. Figure 2.9 depicts an airfoil with a certain flow. Flow separation occurs at around 80 degrees for a smooth sphere in laminar flow. If the boundary layer is turbulent instead of laminar, it is better able to remain attached to the surface and flow separation is delayed until around 120 degrees, which reduces pressure drag significantly. This is because turbulence introduces a lot of mixing between the different layers of flow and thus momentum transfer means the flow can sustain a larger adverse pressure gradient without separating.

2.8   Active Flow Control

Active and passive flow control is important for delaying flow separation. Active flow control actually adds energy or momentum to air flow in a regulated manner. Hence, active

flow control is energy consumptive. Active flow control techniques can be done by introducing fluidic actuators, plasma actuator or moving surface. One of these techniques is the implementation of additional suction pressure at slot position on upper surface of airfoil to prevent boundary layer separation.

2.9 Passive Flow Control

Passive flow control requires no auxiliary power or control loop. It involves geometry shaping, use of vortex generators or grooves in the form of riblets and waves in the longitudinal or transverse direction to the flow stream. A passive slot is a custom-designed internal slot on the airfoil surface that helps to achieve better aerodynamic performance. It permits high pressure flow to pass from pressure side to suction side of airfoil to increase the momentum of boundary layer in support of delaying flow separation and stall.

2.10 Airfoil Nomenclature

The NACA airfoils are the earliest standardized and reliable airfoil shapes for aircraft wings developed by the National Advisory Committee for Aeronautics (NACA). Airfoils are described and can be distinguished between each other by the numbers that follow the acronym NACA. There are six NACA families which are 4- Digit, 5-Digit, 6-Series, 7-Series, 8-Series and 16-Series. The airfoil used in this work is NACA 0018 which belongs to the first family of airfoil in the NACA 4-Digit series. In NACA Four Digit Series, there are four digits that follow the acronym NACA and these 4 digits show 3 different properties of the airfoil. The explanation of the 4-digit NACA airfoil (NACA 0018) of the present study is as follows [35, 36]:

- NACA stands for National Advisory Committee for Aeronautics.

- The first digit, 0 specifies the maximum camber (m) in percentage of the chord i.e zero camber (symmetric airfoil).

- The second digit indicates the position of the maximum camber (p) in tenths of chord i.e. 0% chord length.

- The last two digits provide the maximum thickness (t) of the airfoil in fractional percentage of the chord length i.e 18% thickness to chord length ratio.

The equations for a NACA 4-digit symmetric airfoil is given below:

$$\pm y_t = 5tc \left(0.2969 \sqrt{\tfrac{x}{y}} - 0.1260 \tfrac{x}{c} - 0.3516 \left(\tfrac{x}{c}\right)^2 + 0.2843 \left(\tfrac{x}{c}\right)^3 - 0.1015 \left(\tfrac{x}{c}\right)^4 \right) \tag{2.4}$$

Where c is the chord length, x is the position along the chord from 0 to c, y_t is the half thickness at a given value of x (centerline to surface) and t is the maximum thickness as a fraction of the chord in percentage.

Equation (2.4) gives the shape of the airfoil with the thickness distribution above (+) and below (–) the chord line when the value of t is substituted into it for each x coordinate. The coordinates of the upper airfoil surface (x_U, y_U) and the lower airfoil surface (x_L, y_L) are expressed as: $x_U = y_U = x$, $y_U = +y_t$ and $y_L = -y_t$.

By default symmetrical 4-digit series airfoils have maximum thickness at 30% of the chord from the leading edge.

2.11   Use of NACA 0018 Airfoil

NACA 0018 is a symmetric airfoil, developed by U.S. National Aviation Advisory Board was selected in this study as the object for the numerical analysis. Symmetrical airfoils produce less lift in comparison to cambered airfoil but aid more in aerobatics and maneuverability of an aircraft. Symmetrical NACA 0018 airfoil is used in small-to-medium scale vertical-axis wind turbines and aerial vehicles.

COMPUTATIONAL METHOD

3.1 Fundamental Equation

The governing equations for the present study are the continuity equation and momentum equation. Both the mass and momentum equation constitute the Navier-Stokes equations. These equations for two-dimensional flow can be expressed as follows:

- Conservation of mass:

$$\frac{\partial(\rho u)}{\partial x} + \frac{\partial(\rho v)}{\partial y} = 0 \tag{3.1}$$

- Conservation of momentum:

X-momentum: $\rho\,(u\frac{\partial u}{\partial x} + v\frac{\partial u}{\partial y}) = -\frac{\partial p}{\partial x} + \mu(\frac{\partial^2 u}{\partial x^2} + \frac{\partial^2 u}{\partial x^2}) + \rho g_x$ (3.2)

Y-momentum: $\rho\,(u\frac{\partial v}{\partial x} + v\frac{\partial v}{\partial y}) = -\frac{\partial p}{\partial y} + \mu(\frac{\partial^2 v}{\partial x^2} + \frac{\partial^2 v}{\partial x^2}) + \rho g_y$ (3.3)

The Navier-Stokes equations are very robust. They can solve any type of fluid flow problem ranging from slow viscous creeping flow, Non-Newtonian flows and also turbulent flows. Turbulent flows are everywhere in nature and engineering. Turbulence involves a lot of scales from tiny scales of motion to scales of motion that are of order of the domain. This range of scales is dependent on a non-dimensional number called Reynolds number. To solve this scale domain, the domain has to be discretized very finely and the computational cost is immense. This type of solving is called Direct Numerical Solution (DNS) where the Navier-Stokes equations are solved completely. The expected computational time for DNS is of the order of R_e^3. The Reynolds number of many real life applications like an aircraft is R_e^5. This makes it impossible to perform a DNS study on it. To overcome this problem, various techniques such as RANS, LES have been introduced.

Reynolds Average Navier Stokes (RANS) equations are time averaged equation of fluid flow. In this method all instantaneous quantities like velocity is decomposed into its time averaged and fluctuating quantities. When we apply time averaging and decompose these instantaneous quantities into its average and fluctuating components, we obtain the Reynolds average

momentum equation. In this equation, there is a non-linear term known as Reynolds stress. To obtain the solution, this model has to be modeled. The modeling of this Reynolds stress is very essential to obtain closed form solution and to come up with this model for this Reynolds stress term, various techniques have been developed like zero equation model, standard k-ω model, RNG k-ω model, Realizable k-ω model, SST k-ε model, Standard k-ε model, Spalart- Allmaras turbulence model.

In this present study, Spalart- Allmaras turbulence model [37] is used. This turbulence model helps to make the Reynolds-averaged Navier-Stokes equations solvable, and it is available in some commercial field solvers. The model was specifically derived for use in aerodynamic applications involving wall-bounded systems as well as in turbo-machinery applications. The model includes multiple parameters and coefficients as part of a simulation, but because there is only one dynamic differential equation to solve, it is computationally much simpler than a DNS approach.

In particular, this one-equation model allows simpler resolution of the eddy viscosity near a system boundary (such as a wall). Hence, it is a relatively simple RANs one-equation model that solves a modeled transport equation for the kinematic eddy (turbulent) viscosity, $\tilde{v}$. This embodies a relatively new class of one-equation models in which it is not necessary to calculate a length scale related to the local shear layer thickness. The Spalart- Allmaras turbulence model follows a single dynamic equation describing a kinematic viscosity like variable. The transported variable in the Spalart-Allmaras model, $\tilde{v}$ is identical to the turbulent kinematic viscosity except in the near-wall (viscosity-affected) region. The transport equation for $\tilde{v}$ is:

$$\frac{\partial}{\partial t}(\rho\tilde{v}) + \frac{\partial}{\partial x_i}(\rho\tilde{v}u_i) = G_v + \frac{1}{\sigma_{\tilde{v}}}\left[\frac{\partial}{\partial x_j}\left\{(\mu + \rho\tilde{v})\frac{d\tilde{v}}{dx_j}\right\} + C_{b2\rho}\left(\frac{\partial\tilde{v}}{\partial x_j}\right)^2\right] - Y_v + S_{\tilde{v}} \qquad (3.4)$$

Here, G_v is the production of turbulent viscosity, and Y_v is the destruction of turbulent viscosity that occurs in the near-wall region due to wall blocking and viscous damping. $\sigma_{\tilde{v}}$ and C_{b2} are the constants and v is the molecular kinematic viscosity. $S_{\tilde{v}}$ is a user-defined source term. The goal in this above equation is to determine the turbulent eddy viscosity. The turbulent viscosity, μ_t is computed from:

$$\mu_t = \rho\tilde{v}f_{v1} \qquad (3.5)$$

where the viscous damping function, f_{v1} is given by:

$$f_{v1} = \frac{X^3}{X^3 + C_{v1}^3} \text{ and } X \equiv \frac{\tilde{v}}{v}$$

(3.6)

In these equations, the molecular kinematic viscosity is $v = \mu/\rho$, the fluid density is ρ, and μ is the fluid's molecular dynamic viscosity. The other parameters in the model are given in terms of the distance from the field point to the nearest wall d.

The production term, G_v is modeled as:

$$G_v = C_{b1\rho}\tilde{S}_v$$

(3.7)

where

$$\tilde{S} \equiv S + \frac{\tilde{v}}{k^2 d^2} f_{v2}$$

(3.8)

$$f_{v2} = 1 - \frac{X}{1 + X f_{v1}}$$

(3.9)

C_{b1} and k are constants, d is the distance from the wall, and S is a scalar measure of the deformation tensor. By default in ANSYS FLUENT, as in the original model proposed by Spalart and Allmaras, S is based on the magnitude of the vorticity:

$$S \equiv \sqrt{2\Omega_{ij}\Omega_{ij}}$$

(3.10)

Where Ω_{ij} is the mean rate-of-rotation tensor and is defined by

$$\Omega_{ij} = \frac{1}{2}\left(\frac{\partial u_i}{\partial x_j} - \frac{\partial u_j}{\partial x_i}\right)$$

(3.11)

The destruction term is modeled as:

$$Y_v = C_{w1\rho} f_w \left(\frac{\tilde{v}}{d}\right)^2$$

(3.12)

Where

$$f_w = g \left[\frac{1 + C_{w3}^6}{g^6 + C_{w3}^6}\right]^{1/6}$$

(3.13)

$$g = r + C_{w2}(r^6 - r)$$

(3.14)

$$r \equiv \frac{\tilde{v}}{\tilde{S}_k^2 d^2}$$

(3.15)

$\tilde{S}$ is given by equation (3.8). The model constants $C_{b1}, C_{b2}, C_{v1}, C_{w1}, C_{w2}, C_{w3}, \tilde{\sigma}_v$ and k have the following default values:

$C_{b1} = 0.1355,$ $\qquad C_{b2} = 0.622,$ $\qquad \tilde{\sigma}_v = \frac{2}{3},$ $\qquad C_{v1} = 7.1$

$C_{w1} = \frac{C_{b1}}{k^2} + \frac{1 + C_{b2}}{\tilde{\sigma}_v},$ $\qquad C_{w2} = 0.3,$ $\qquad C_{w3} = 2.0,$ $\qquad k = 0.4187$

21

3.2   Discretization Using Finite Volume Method

The main theme of CFD is to create a discrete domain through grid by breaking down a huge volume of fluid into smaller volume of elements. Each flow variable is defined at every point in the continuous domain. In computational fluid dynamics, only at the grid points, one would directly solve for the relevant flow variables. Values of other location are formed by interpolating the value at the grid points. The governing PDEs and boundary conditions are defined as continuous variables p, V etc. In the discrete domain, these variables can be named as discrete variable P_i, V_i etc. This discrete system is a huge set of coupled algebraic equation in the discrete variables. Setting up this discrete system at solving, it requires a huge number of repetitive calculations. To derive the discrete equation by using Taylor's series expansions is known as finite difference method. However, most commercial CFD codes use the finite volume or finite element methods that are best suited for modeling flow past complex geometries. In this current study, the most popular CFD package ANSYS FLUENT is used which evaluates the solutions of the governing partial differential equations using finite volume method.

The Finite Volume Method (FVM) is a discretization process for the approximation of a single or a system of partial differential equations expressing the conservation or balance of one or more quantities. Finite volume method is a method based on integral approach. Considering the PDE with no production terms with time and space derivative can be written separately as:

$u_t + f_x(u) = 0$, where $f_x(u)$ represents flux terms. Since FVM is based on integral approach, so the integral arrives as:

$$\int_{x_{i-1/2}}^{x_{i+1/2}} u_t \, dx + \int_{x_{i-1/2}}^{x_{i+1/2}} f_x(u) \, dx = 0 \qquad ((3.16)$$

Here the region of integration is taken to be a control volume associated with the point of coordinate x_i, represented by $x_{i-1/2} \leq x \leq x_{i+1/2}$.

After approximating the first integral using the mid-point rule, the semi-discrete form arrives as:

$$|u_t|_i(x_{i+1/2} - x_{i-1/2}) + f(u_{i+1/2}) - f(u_{i-1/2}) = 0 \qquad (3.17)$$

This approach produces a conservative scheme since we are matching the flux crossing the boundary of one finite volume to the adjacent volume. So in finite volume method it is very crucial to assess the flux crossing the boundaries.

Finite volume method (FVM) has two major advantages. First, it enforces conservation of quantities at discretized level, i.e. mass, momentum, energy remain conserved also at a local scale. Fluxes between adjacent control volumes are directly balanced. Secondly finite volume schemes take full advantage of arbitrary meshes to approximate complex geometries.

3.3   Geometry of the Present Study

The chord length of 1m as illustrated in Figure 3.1 is chosen as the profile of baseline airfoil where the upper surface of the profile is defined as the suction surface and lower side is defined as the pressure surface.

Suction surface

Pressure surface
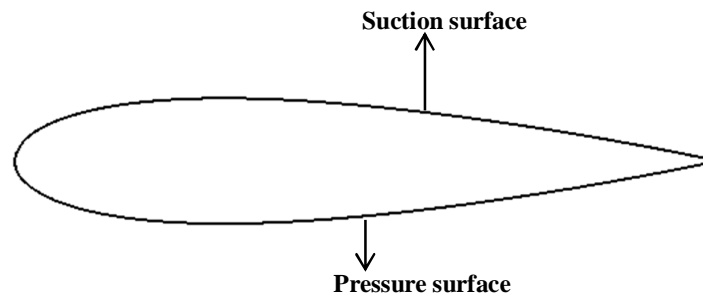
Figure 3.1: 2D baseline airfoil

The computational domain is shown in Figure 3.2.The domain is expanded 10C above and below the airfoils to make sure that confinement effects are negligible.

Symmetry

10C

Velocity
Inlet

Pressure
Outlet

10C

20C

10C

Symmetry
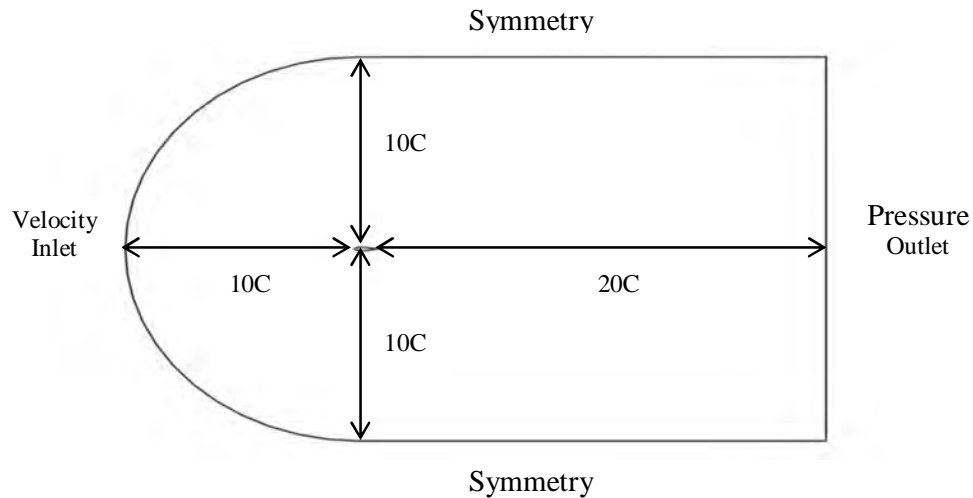
Figure 3.2: Computational domain

23

Then the domain is expanded far enough upstream (10C) and downstream (20C) such that the inlet and outlet boundaries do not affect the flow near the airfoil. Inlet and outlet boundary conditions are chosen as velocity inlet with uniform inflow and pressure outlet with zero gauge pressure. Symmetry boundary conditions are chosen for upper and lower boundary.

A slot of width 2% of the chord length is placed at four different locations such as 40%, 50%, 60% and 70% of chord length on the upper surface of the airfoil. Aerodynamic performance is computed by introducing suction pressure on definite slot position.

The geometry of the airfoil profile with the suction slot at 70% chord length position is given below:

(a)

(b)
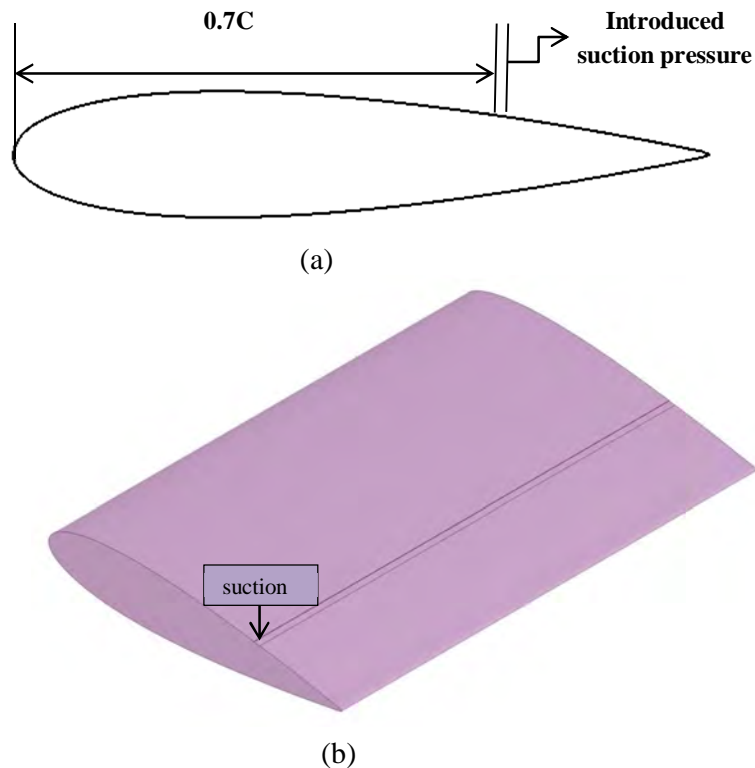
Figure 3.3: Geometry of (a) 2D and (b) 3D baseline airfoil with suction pressure at 70% chord length slot position

Two different configurations of internal slots are introduced as passive flow control mechanism. First configuration is leading edge chordal slot that has a uniform width of 2% of the chord length. It exits from top surface of the airfoil and it is inclined to an angle of 120° with respect to the chord line. In the second configuration, the internal slot of 2% chord length is placed tangentially at four different chord lengths such as 30%, 40%, 50% and 60% of the chord length on the upper surface of the airfoil.

24

Figure 3.4 shows the geometry of the airfoil profile with leading edge chordal slot at 30% chord length position.

(a)

(b)
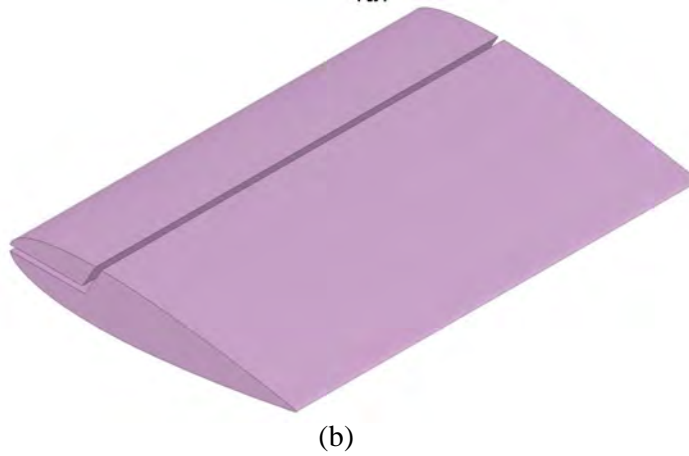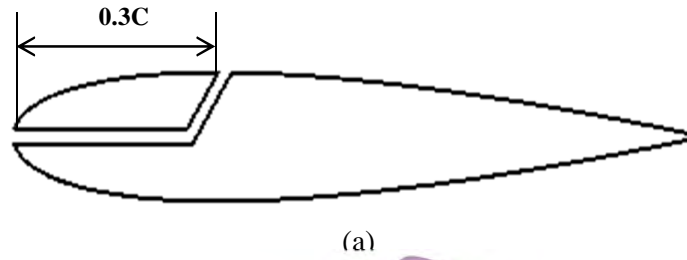
Figure 3.4: Geometry of (a) 2D and (b) 3D baseline airfoil with leading edge chordal slot at 30% chord length slot position

(a)

(b)
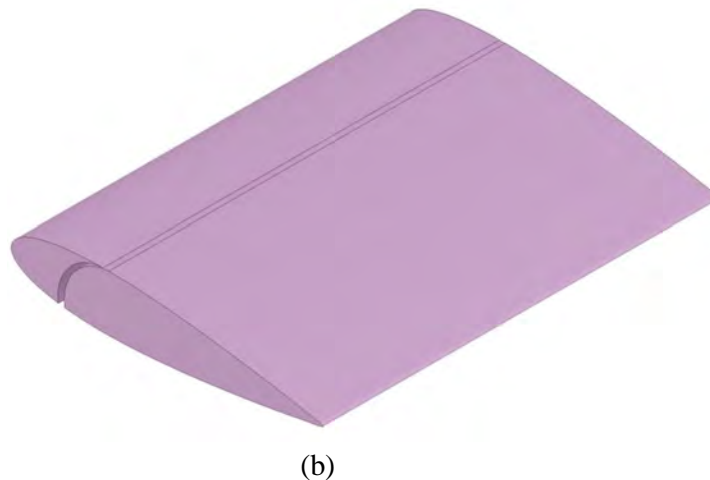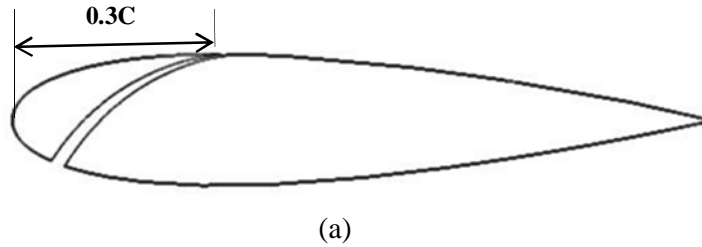
Figure 3.5: Geometry of (a) 2D and (b) 3D baseline airfoil with tangential internal slot at 30% chord length slot position

Figure 3.5 shows the geometry of the airfoil profile with tangential internal slot at 30% chord length position.

The combined effect of suction and internal slot is made with the second configuration of internal slot at 30% of the chord length position and introduced suction pressure at 70% of the chord length position.

The geometry of the airfoil profile with the combination of suction and internal slot is given below in Figure 3.6.

(a)

(b)
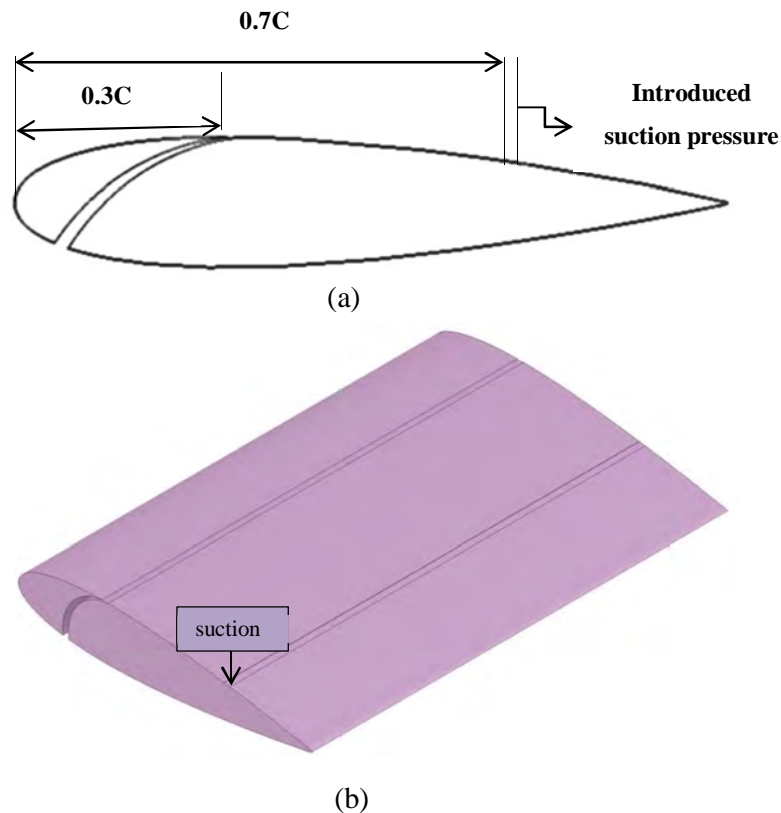
Figure 3.6: Geometry of (a) 2D and (b) 3D baseline airfoil with the combination of suction and tangential internal slot

3.4   Tools Used

CFD simulations are done by using commercial software packages. The chosen airfoil is generated by using SOLIDWORKS 2018. Then the profile is imported into ANSYS 18.1 FLUENT. Then the FLUENT is used here to do all the pre-processing including generating meshes, quality control and setting up boundary conditions for all the airfoil configurations. Finite volume method is used to analyze CFD model by FLUENT. FLUENT is a finite

volume method which illustrates and analyzes PDEs (Partial Differential Equations) of algebraic equation. So, it is a CFD tool which is used to solve governing equation of conservation of mass and momentum.

3.5   Grid Generation

Grid generation is a complex part in computational fluid dynamics simulation and it is used to indicate both the simulation time and accuracy of the desired result. In the current study, meshing or discretization of domain is performed with the help of ANSYS meshing software 18.1. The present mesh is confirmed by grid independence test which is used to check the optimism of the grid. If the result does not varied that much with the increment of element numbers, then it means the result is no more dependent on element number. This process can be referred as Grid Independence Test. The grid independence test is carried out on the numerical result of plain airfoil at R_e = 7.12 x10^6 and 17° angle of attack for three different grid sizes such as 30,000, 40,200, 60,000 and 72,000 elements. This independence analysis is done for plain airfoil since the same domain size is used for the numerical study of modified airfoil. Hence, the grid sizes are approximately same.

Table 1: Grid Independency Test at 17° Angle of Attack and R_e = 7.12x10^6

Number of Elements	Lift coefficient	Drag coefficient
30,000	1.3976	0.04153
40,200	1.4183	0.03989
60,000	1.4279	0.03819
72,000	1.4290	0.03848

Table 1 shows that refinement of the grid size from 30,000 to 40,200 cells which lead to a difference in the lift coefficient and drag coefficient values (1.48% and 3.95% respectively). Further increment in grid size to 60,000 and later to 72,000 results in a negligible difference in the lift and drag coefficients values. For reducing the calculation time optimum grid size 60,000 cells is taken here. The grid has high impact on convergence, accuracy and solving time. This is the reason of selecting grid numbers carefully for the perfection of the result and minimal solving time which leads to optimum grid selection.

The cell or element should be supported by the solver. ANSYS FLUENT supports triangle or quadrilateral elements in 2D and tetrahedral, hexahedra, pyramid and prism elements in 3D. In present 2D simulation process, quadrilateral element is used which is referred as quad element.

There are many grid generation processes for the creation of high quality grid within small amount of time. All the methods are broadly divided into three categories namely;

- Cartesian grid generation methods,
- Structured grid generation methods
- Unstructured grid generation methods
- Hybrid grid generation methods

Current 2D meshing is done using structured mesh where elements follow structured pattern.

3.6 Meshing

Meshing is the process in which the continuous geometric space of an object is broken down into thousands or more of shapes to properly define the physical shape of the object. Meshing, also known as mesh generation, is the process of generating a two-dimensional and three-dimensional grid; it is dividing complex geometries into elements that can be used to discretize a domain. Since meshing typically consumes a significant portion of the time in acquiring simulation results, advanced automated meshing tools can provide faster and more accurate solutions. Meshing is very important factor for the high quality of CFD simulation.
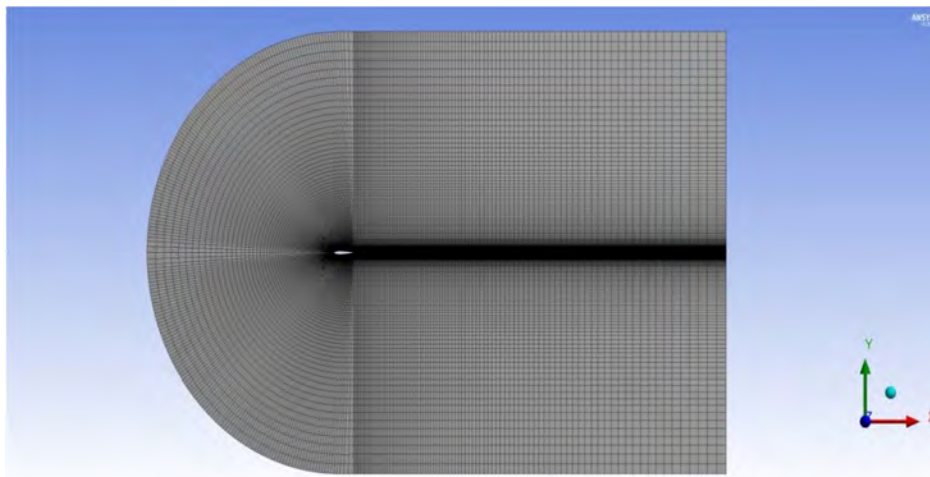
Figure 3.7: Meshing domain for 2D airfoil

Figure 3.7 shows the meshing domain of the present study with a closer view of mesh around the airfoil. Here, a 2D structured mesh is integrated with total number of cells about 60,000 in the airfoil.

In order to capture the pressure gradients, velocity gradients and flow separation near the airfoil boundary, the mesh is created by placing sufficient inflation cells within the boundary layer. Size of the element is decided by y^+ which is a non-dimensional wall normal distance or in simple words it is the height of the first step next to airfoil surface. It determines the accuracy of the boundary layer capture and this in turn determines the accuracy of the forces. Ideally the value of y^+ should be around 1 which can accurately capture the boundary layer but this also means that the number of elements in the mesh is very high which will result in very long computational time.

In actual practice, it is very difficult to achieve y^+ around 1 and it needs high computational resources. The other option is to have a y^+ in between 30 to 300. This means that the boundary wall is not resolved but in this case the wall function is used. When the y^+ is not around 1, it means it is essentially loosing information in the boundary layer. This information can be captured using wall function. For standard wall functions, each wall-adjacent cell's centroid should be located within the log-law layer, $30<y^+<300$. It is important in turbulence modeling to determine the proper size of the cells near domain wall.

Spalart-Allmaras turbulence model is designed to be used with meshes that properly resolve the viscosity affected region, and the damping functions have been built into the model to attenuate turbulent viscosity in the viscous sub-layer. To achieve the best results with the Spalart-Allmaras model a mesh with $y^+ \geq 30$ should be used. For the present study, the height of the first cell adjacent to the surface is set to $1\text{x}10^{-4}$ m, corresponding to a y+ of approximately 30 that is consistent with Spalart-Allmaras turbulence model. Zoomed in views of the meshing near the airfoil surfaces is given in Figure 3.8.

Figure 3.8: Mesh around baseline airfoil

29

3.7   Meshing for Slot with Suction pressure at Different Location of Chord Length

To acknowledge the meshing procedure for all the slots with suction pressure, the meshing of 70% chord length slot position for suction is given below in Figure 3.9:
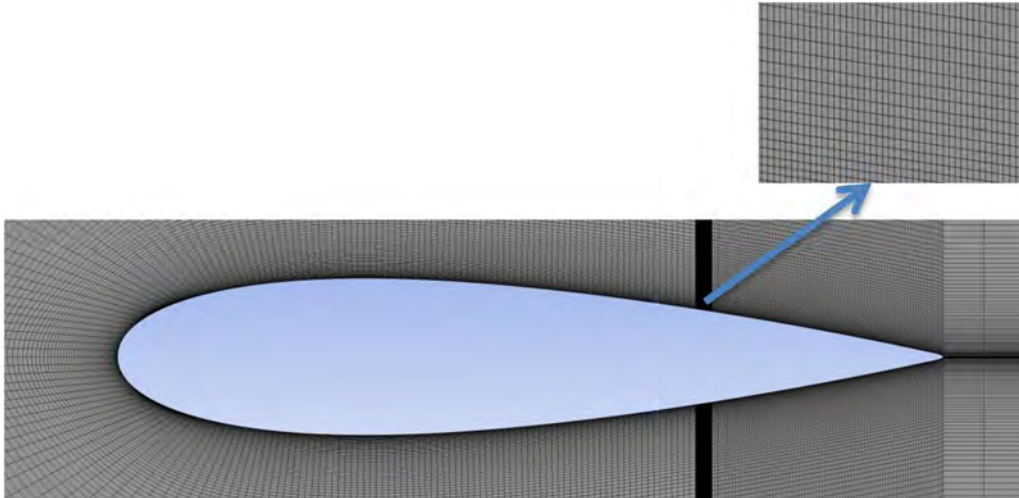
Figure 3.9: Magnified view of meshing at 70% chord length slot position for suction

3.8   Meshing for Leading Edge Chordal Slot

To acknowledge the meshing procedure for leading edge chordal slot, the magnified view of meshing of 30% chord length slot position is presented in Figure 3.10. It exits from top surface of airfoil that is inclined to an angle of 120° with respect to chord line.
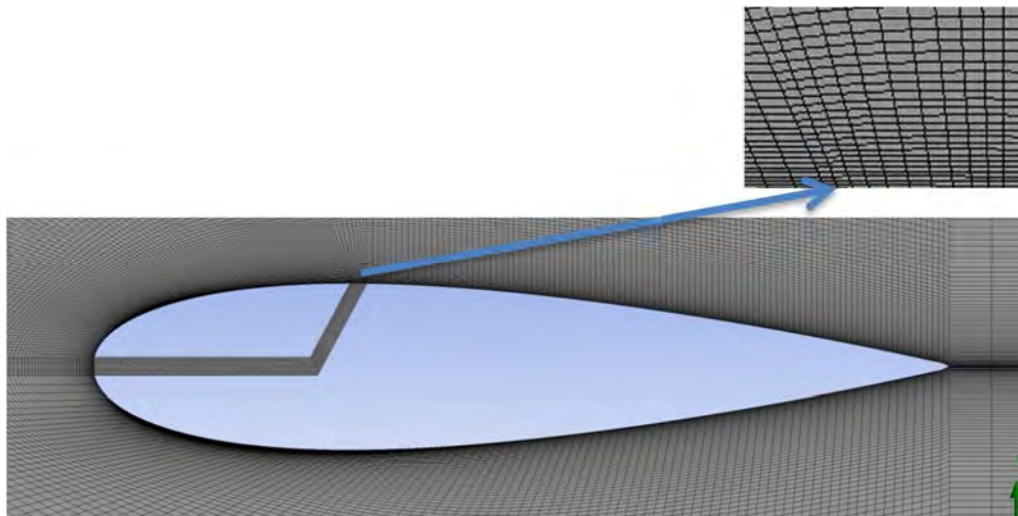
Figure 3.10: Magnified view of meshing at 30% chord length position for leading edge chordal slot

3.9   Meshing for Tangential Internal Slot at Different Location of Chord Length

To understand the meshing procedure of all the considered tangential internal slot positions, meshing of 30% chord length internal slot position is given in Figure 3.11:
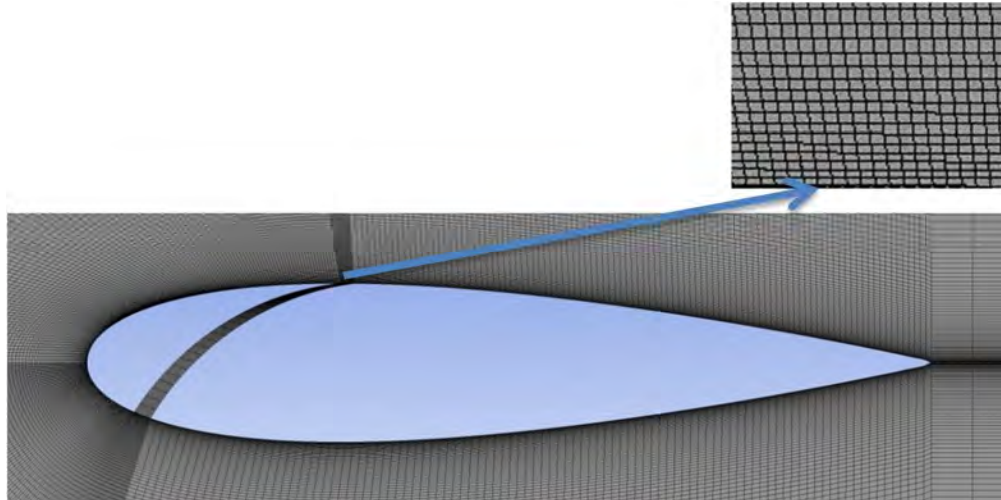
Figure 3.11: Magnified view of meshing at 30% chord length position for tangential internal slot position

3.10   Meshing for Combined Effect of Slot with Suction Pressure and Tangential Internal Slot

To acknowledge the meshing procedure of the combined effect of slot positions along with suction pressure on NACA 0018 the airfoil, magnified view of meshing is shown in Figure 3.12.
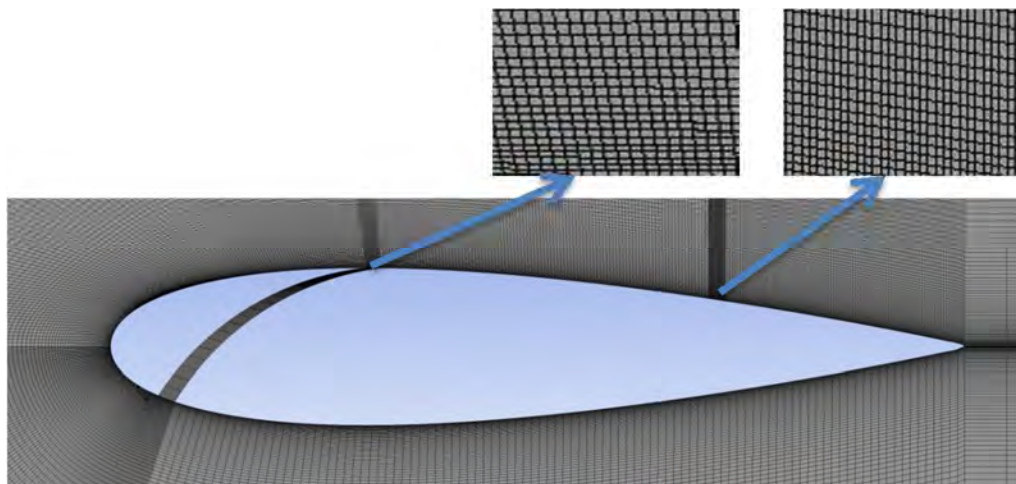
Figure 3.12: Magnified view of meshing of combined effect of 70% chord Length slot position with suction pressures and 30% chord length tangential internal slot position

3.11   Solver Setting

ANSYS FLUENT as CFD tool is used to solve the governing integral equations for the conservation of mass and momentum. By modifying the solver settings, the rate of convergence of the simulation and the accuracy of the computed result can be improved. The following solver setting is used for the current simulation:

Solver	Velocity formulation	2D space	Time
Pressure based	Absolute	Planar	Steady

3.12   Pressure Based Solver

To solve any computational problem, ANSYS Solver uses finite volume method. It is mainly focused to transform the partial differential equations to linear algebraic equations in a discretized form. This is where Euler and Navier equations come into play for solving the problem. Basically, there are two solvers (i) Pressure based and (ii) density based.

The pressure-based solver traditionally has been used for incompressible and mildly compressible flows [38]. The density-based approach, on the other hand, was originally designed for high-speed compressible flow.

The pressure-based solver employs an algorithm which belongs to a general class of methods called the projection method. In the projection method, the constraint of mass conservation (continuity) of the velocity field is achieved by solving a pressure (or pressure correction) equation. The pressure equation is derived from the continuity and the momentum equations in such a way that the velocity field, corrected by the pressure, satisfies the continuity. Since the governing equations are nonlinear and coupled to one another, the solution process involves iterations wherein the entire set of governing equations is solved repeatedly until the solution converges.

The pressure-based solver allows solving the flow problem in either a segregated or coupled manner. ANSYS FLUENT provides the option to choose among five pressure-velocity coupling algorithms: SIMPLE, SIMPLEC, PISO, Coupled, and (for unsteady flows using the non-iterative time advancement scheme (NITA)) Fractional Step (FSM). All the aforementioned schemes, except the "coupled" scheme, are based on the predictor-corrector

approach. SIMPLE, SIMPLEC, PISO, and Fractional Step use the pressure-based segregated algorithm, while Coupled uses the pressure-based coupled solver. Using the coupled approach offers some advantages over the non-coupled or segregated approach. The coupled scheme obtains a robust and efficient single phase implementation for steady-state flows, with superior performance compared to the segregated solution schemes. This pressure-based coupled algorithm offers an alternative to the density-based and pressure-based segregated algorithm with SIMPLE-type pressure-velocity coupling.

The coupled algorithm solves the momentum and pressure-based continuity equations together. The full implicit coupling is achieved through an implicit discretization of pressure gradient terms in the momentum equations, and an implicit discretization of the face mass flux, including the Rhie-Chow pressure dissipation terms. In the momentum equations, the pressure gradient for component k is of the form:

$$\sum_f p_f A_k = -\sum_j a^{u_k p} P_j \qquad (3.18)$$

Where, p_f is the pressure values at the faces, $a^{u_k p}$ is the coefficient derived from the Gauss divergence theorem and coefficients of the pressure interpolation schemes. Finally, for any i^{th} cell, the discretized form of the momentum equation for component u_k is defined as:

$$\sum_j a_{ij}^{u_k u_k} u_{kj} + \sum_j a_{ij}^{u_k P} p_j = b_i^{u_k} \qquad (3.19)$$

In the continuity equation, the balance of fluxes is replaced using the flux expression resulting in the discretized form:

$$\sum_k \sum_j a_{ij}^{p u_k} u_{kj} + \sum_j a_{ij}^{pp} p_j = b_i^p \qquad (3.20)$$

As a result, the overall system of equations (3.19) and (3.20), after being transformed to the δ-form, is presented as:

$$\sum_j [A]_{ij} \vec{X}_j = \vec{B}_i \qquad (3.21)$$

where the influence of a cell i on a cell j has the form:

$$A_{ij} = \begin{bmatrix} a_{ij}^{pp} & a_{ij}^{pu} & a_{ij}^{pv} & a_{ij}^{pw} \\ a_{ij}^{up} & a_{ij}^{uu} & a_{ij}^{uv} & a_{ij}^{uw} \\ a_{ij}^{vp} & a_{ij}^{vu} & a_{ij}^{vv} & a_{ij}^{vw} \\ a_{ij}^{wp} & a_{ij}^{wu} & a_{ij}^{wv} & a_{ij}^{ww} \end{bmatrix} \qquad (3.22)$$

and the unknown and residual vectors have the form:

$$\vec{X}_j = \begin{bmatrix} p'_i \\ u'_i \\ v'_i \\ w'_i \end{bmatrix} \qquad (3.23)$$

$$\vec{B}_i = \begin{bmatrix} -r_i^p \\ -r_i^u \\ -r_i^v \\ -r_i^w \end{bmatrix} \qquad (3.24)$$

The equation (3.21) is solved using the coupled algebraic multi grid. In this equation the matrix is algebraically associated with a uni-dimensional unknown vector. The product of both matrices is then equivalent to a solution vector where boundary conditions are included.

With this coupled algorithm, each iteration consists of the steps illustrated in Figure 3.13:
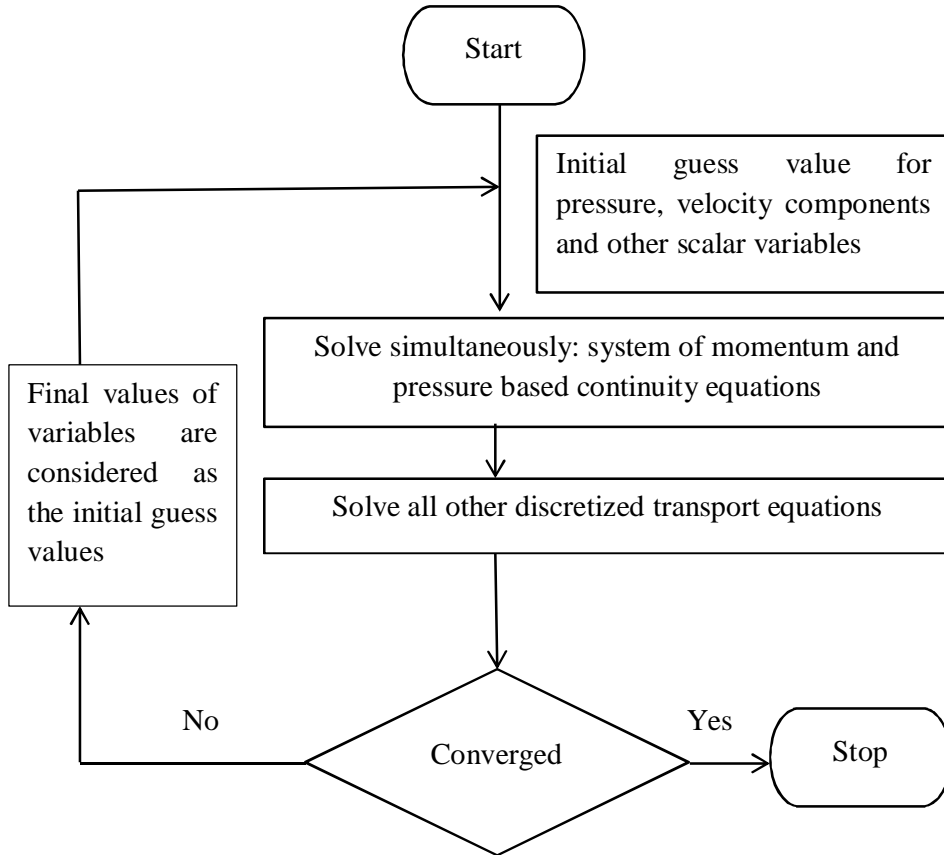
Figure 3.13: Algorithm for pressure based coupled solver

RESULTS AND DISCUSSIONS

4.1   Validation

CFD simulation results need to be validated with earlier proven reference data. Validation process is done with 2D experimental investigation by Timmer [39] in 2008. Here calculated results are validated with the experimental results at $R_e = 0.3 \times 10^6$ for NACA 0018 airfoil.
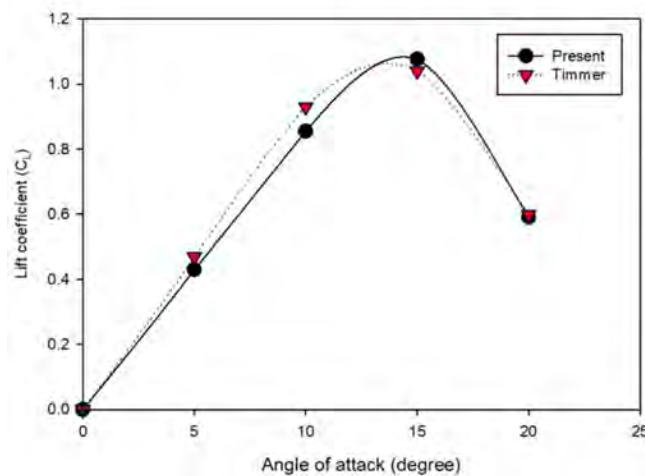
Figure 4.1: Comparison of the calculated lift coefficient of present model with the experimental data [37] for 2D airfoil at $R_e=0.3 \times 10^6$
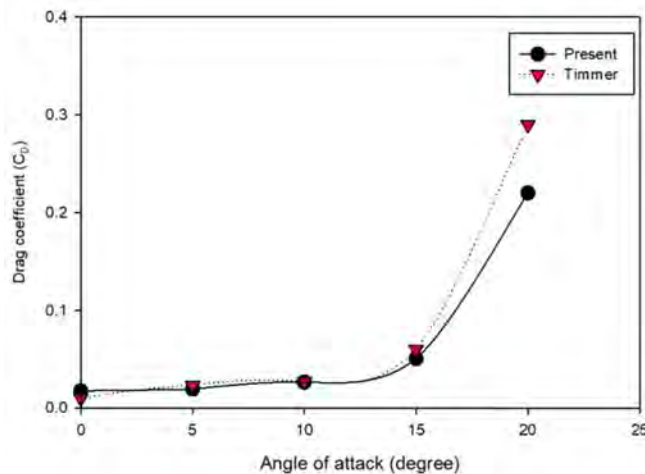
Figure 4.2: Comparison of the calculated drag coefficient of present model with the experimental data [37] for 2D airfoil at $R_e=0.3 \times 10^6$

From Figure 4.1 and Figure 4.2 it is observed that, CFD simulation result agrees well with the experimental data. While considering drag coefficient, the obtained value from simulation differs from experimental investigation after 15° angle of attack. Since the stall angle is below 15° angle of attack, hence we ignore this numerical error. Therefore, this code is used throughout the simulation.

4.2   Determination of Stall Angle of Plain Airfoil

Computational run is performed on 2D airfoil to determine the stall angle of it. The air density, ρ is taken as 1.225 kg/m^3, dynamic viscosity as 1.7894x10^{-5} Ns/m^2 and Reynolds number of 7.12x10^6 based on all the parameters.

The critical angle of attack is the angle of attack which produces the maximum lift coefficient. It is also known as "stall angle of attack". Hence, it can be said that the relation between the angle of attack and the lift coefficient determines the stall angle. Below the critical angle of attack, the lift coefficient increases with the increment of angle of attack while above the critical angle of attack, the lift coefficient decreases with the increment of angle of attack.

Table 2: Values of lift coefficient with different angle of attack for 2D airfoil

Angle of attack	Lift coefficient (C_L)
0°	0.000002614
5°	0.50624
10°	1.0281
15°	1.3833
16°	1.4148
17°	1.4279
18°	1.4081
19°	1.3392
20°	1.2141

Table 2 shows the values of lift coefficient with the increment of angle of attack and Figure 4.3 shows the graphical representation of these values.
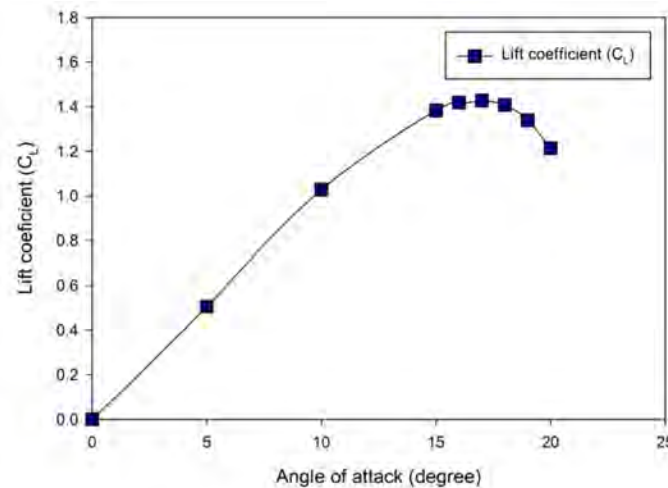
Figure 4.3: Variation of lift coefficient with angle of attack for plain airfoil

In Figure 4.3, lift coefficient is zero for 0° angle of attack. The value of lift coefficient increases with the increase of angle of attack up to 17° angle of attack and after that the lift coefficient decreases gradually due to the flow separation on upper surface of the airfoil. Hence, the stall condition occurs at 17° angle of attack for this case.

4.3 Suction Position Selection on Airfoil

Suction position selection is one of the main concerns to enhance the desired aerodynamic performance. Slot with a width of 2% chord length is placed at different locations on the upper surface of the airfoil. Since slot position selection process is connected with numerous factors such as suction pressure, angle of attack (AOA) etc., so to minimize all the complexities, aerodynamic performance is measured on the upper position of the airfoil with 74% introduced suction pressure at a constant angle of attack (AOA) 19°. The velocity contour of without suction and with suction at different position of 2D airfoil are given from Figure 4.4 to Figure 4.9.

In Figure 4.4 if we consider the flow over the upper airfoil surface, it shows that in the initial region, the area of the flow decreases and hence velocity increases. This means that flow gets acceleration in this region. Due to the increase of the velocity, the pressure decreases in the direction of the flow and hence the pressure gradient is negative in the initial region. When the area of the flow starts to increase, the velocity of flow along the direction of air starts to

37

decrease. Due to the decrease of velocity, the pressure increases in the direction of flow and hence the pressure gradient becomes positive.
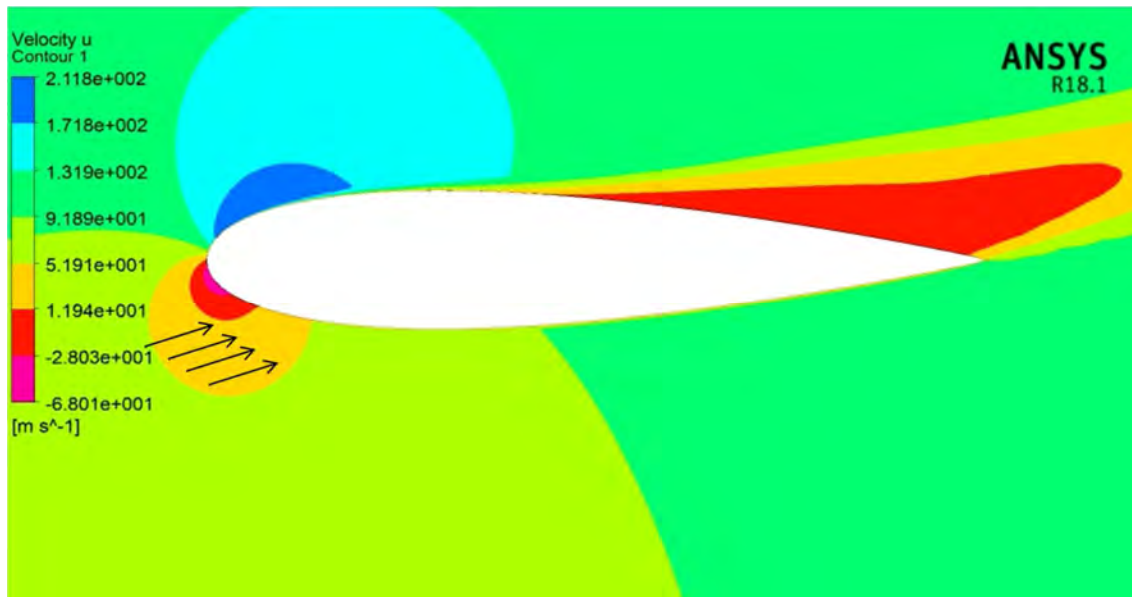
Figure 4.4: u- velocity contour of plain airfoil without suction pressure

The velocity of the layer adjacent to the airfoil surface goes on decreasing as the kinetic energy of the layer is used to overcome the frictional resistance of the surface. Thus the combined effect of positive pressure gradient and surface resistance reduce the momentum of the air. A stage comes, when the momentum of the air flow is unable to overcome the surface resistance. Hence, the flow separation is initiated. At that point the flow takes place in reverse direction and velocity gradient becomes negative near trailing edge as shown in Figure 4.4.
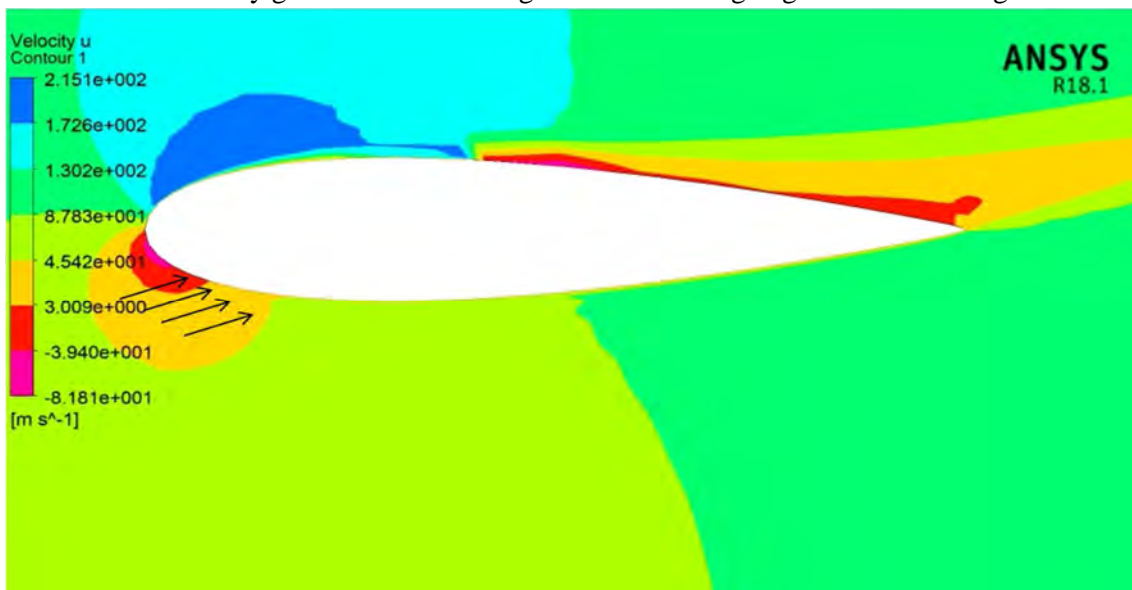
Figure 4.5: u- velocity contour of airfoil with 74% suction pressure at 0.4C slot position

Figure 4.5 shows that the negative velocity gradient region becomes smaller along the upper surface after introducing 74% suction pressure on the 40% chord length slot position. Hence, the presence of flow separation will be lesser in comparison to airfoil without the introduced suction pressure.
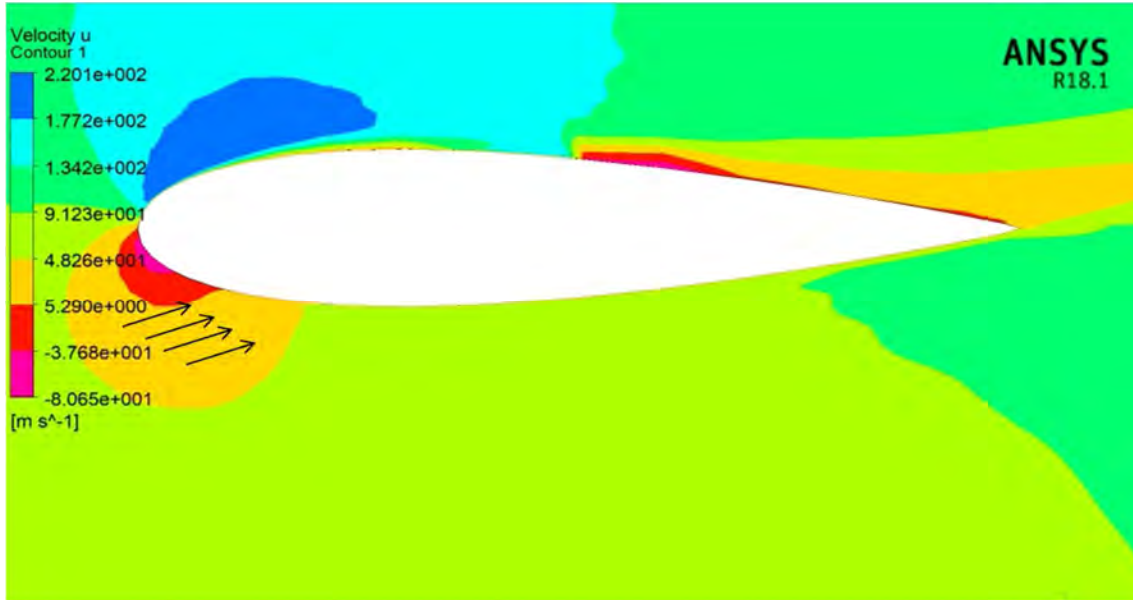
Figure 4.6: u- velocity contour of airfoil with 74% suction pressure at 0.5C slot position

Figure 4.6 shows that the negative velocity region becomes less visible in comparison to Figure 4.5. After introducing suction pressure at 50% chord length slot position, the projection of this negative velocity region starts to diminish towards the trailing edge along the upper surface. Hence the occurrence of flow separation will not be visible at the later part of the trailing edge region.
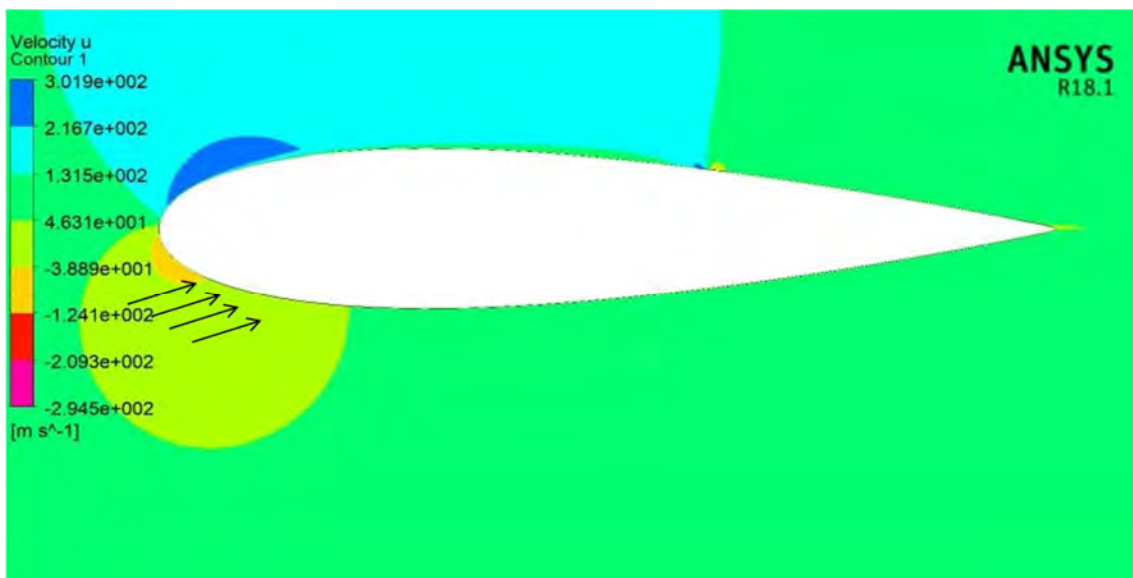
Figure 4.7: u- velocity contour of airfoil with 74% suction pressure at 0.6C slot position

39

Figure 4.7 shows that a negligible or very small area of negative velocity region occurs after introducing suction pressure at 60% chord length slot position. Therefore, it can be said that this slot position will be able to highly subjugate the occurrence of flow separation.
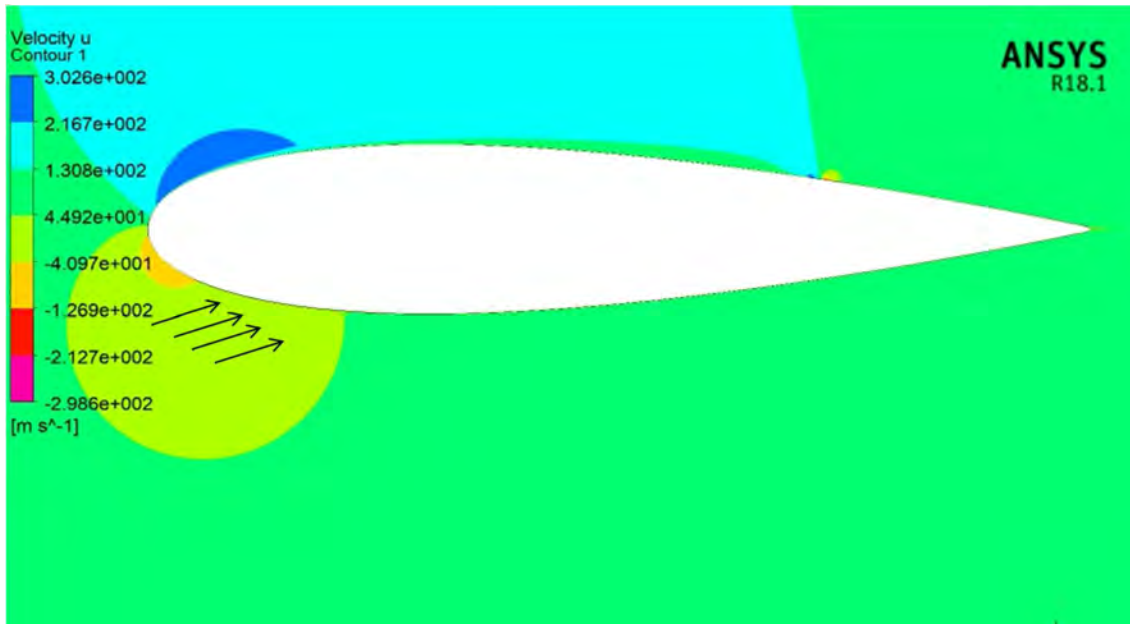
Figure 4.8: u- velocity contour of airfoil with 74% suction pressure at 0.7C slot position

From Figure 4.7 to 4.8, negligible change is found in u-velocity contour profile for 70% chord length slot position comparing with 60% chord length slot position. Hence, this slot position will also be able to control the flow separation effectively.
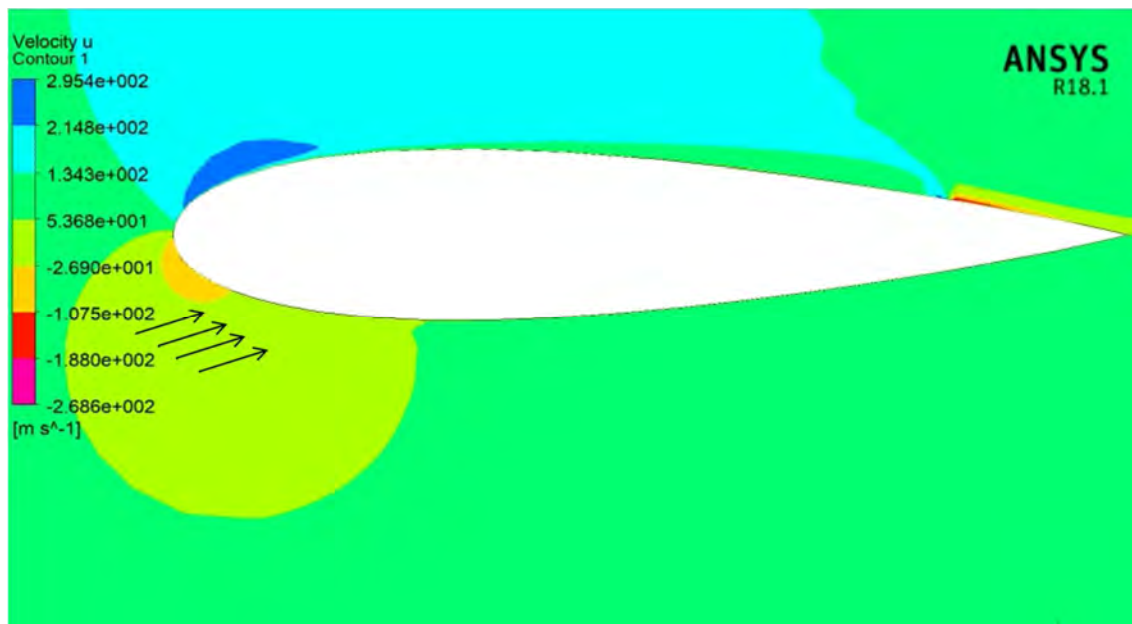
Figure 4.9: u-velocity contour of airfoil with 74% suction pressure at 0.8C slot position

Figure 4.9 shows that the negative velocity region is more visible along the upper surface at 80% chord length slot position in comparison to 60% and 70% chord length slot position. Hence, a small region of flow separation will be visible here after suction at 80% chord length slot position.

The computational runs are conducted for suction slot at 0.4C, 0.5C, 0.6C, 0.7C and 0.8C. Out of these slot positions, effective results are found for 0.6C ~ 0.8C. Therefore, for better presentation the effects on lift to drag ratio for these three suction slots are depicted in compared with no suction slot.
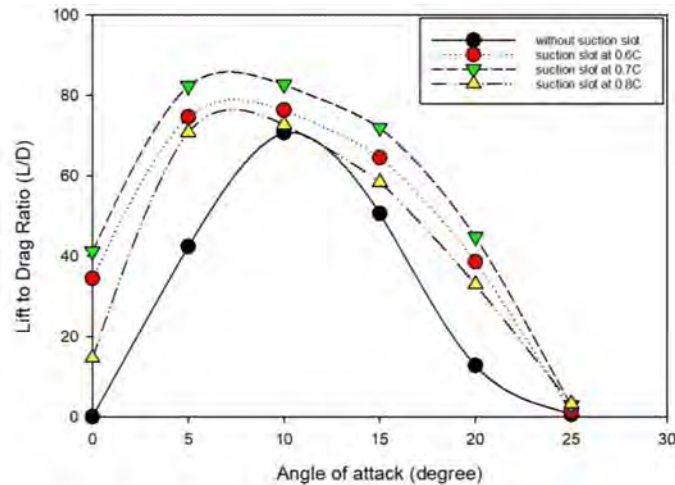
Figure 4.10: Variation of lift to drag ratio for different angle of attack without suction pressure and with 74% suction pressure at 60%, 70% and 80% chord length slot position

The data from Table 3 are plotted as the variation of lift to drag ratio which is shown in above Figure 4.10. This graph shows that among the considered suction positions, the lift to drag ratio is much higher for 70% chord length slot position in comparison to without suction and with suction at 60% and 80% chord length slot position.

4.4   Suction Pressure Selection

While considering higher angle of attacks, lift coefficient increases with the increment of the suction pressure. The data shown in Table 4 are presented in Figure 4.11. From the graph, it can be said that the suction is very much effective at higher angle of attacks with 74% suction pressure.
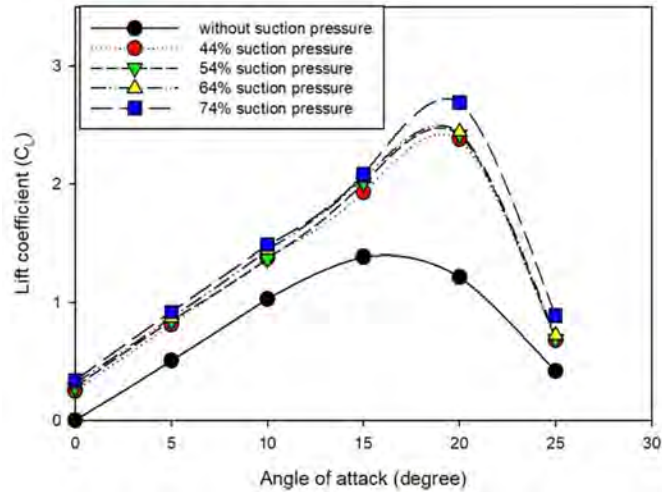
Figure 4.11: Variation of lift coefficient with angle of attack for without and with different suction pressure on 0.7C slot position

Figure 4.12 is the graphical presentation of the data from Table 5 which shows that the suction is not much effective for moderate angle of attacks. At higher angle of attack, suction highly subjugates drag coefficient.
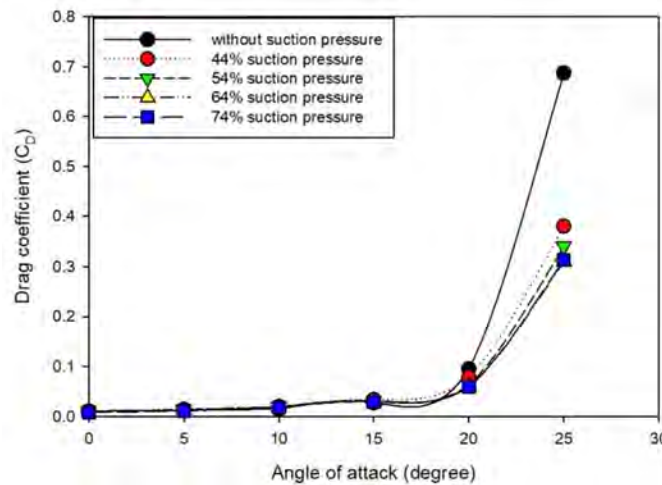
Figure 4.12: Variation of drag coefficient with angle of attack for without and with different suction pressure on 0.7C slot position

Figures 4.11 and 4.12 show that at higher angle of attacks the lift coefficient increases as well as drag coefficient decreases effectively with 74% suction pressure. Hence, stall condition can be delayed with 74% suction pressure at 70% chord length slot position on upper surface of the airfoil.
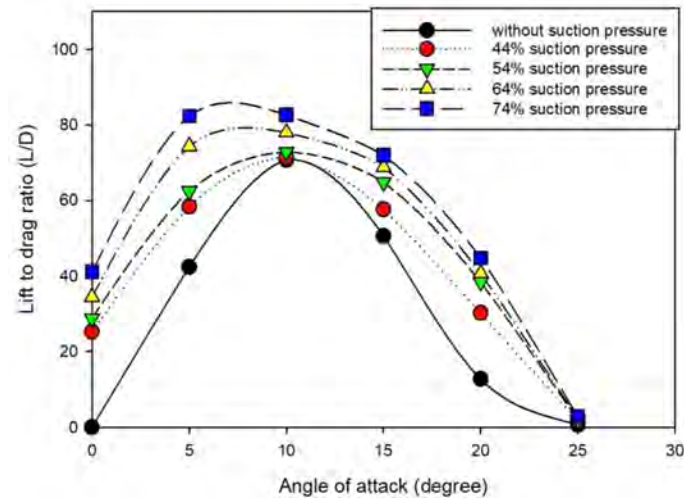
Figure 4.13: Variation of lift to drag ratio with angle of attack for without and with different suction pressure on 0.7C slot position

The data from Table 6 are plotted in Figure 4.13 which shows that for lower angle of attacks the lift to drag ratio increases with the enhancement of suction pressure at 74% than that of without suction. The combination of these occurrences shows that suction is highly acceptable in steady flight at lower angle of attacks and in take-off situation at higher angle of attacks. After introducing suction pressure at 70% chord length position on the upper surface of airfoil, the flow gets reattached. It indicates that the slot sucks the flow into the cavity and results in flow separation delay. Summing up all the above phenomena, it can be said that flow separation can be controlled with 74% suction pressure at slot position of 70% of the chord length on the upper surface of the airfoil.

4.5   Effect of Suction Pressure on Flow Reattachment

The pressure distribution around an airfoil can be divided into two regions: near the leading edge and away from the leading edge. At the first region the highest pressure is obtained at the stagnation point. As the flow expands around the top surface of the airfoil, the surface pressure decreases dramatically, dipping to a minimum pressure which is below the free stream static pressure, P_∞ [40]. When the flow moves farther downstream, the pressure gradually increases, reaching a value above the free stream pressure at the trailing edge. This is known as the unfavorable adverse-pressure gradient region. If the pressure gradient is high enough, then there is a risk of separation phenomena in this region. When the incidence angle

43

increases, the separation of the boundary layer takes place. This causes a wake to form near the trailing edge of the upper airfoil surface and subsequently decreases the lift force and increases the drag force.
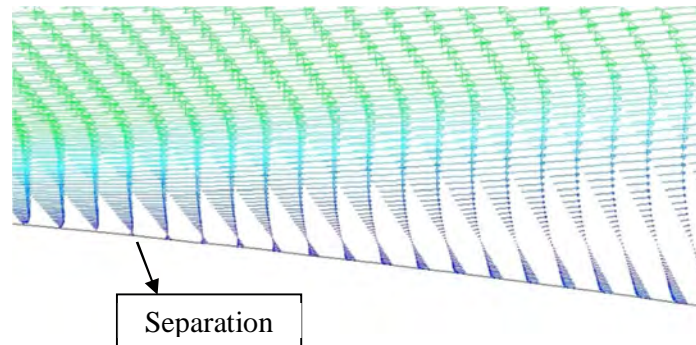
Figure 4.14: Velocity vector at different position of chord length at 19° Angle of Attack

Figure 4.14 shows the closer view of velocity vector profile plain airfoil at 19° angle of attack. The flow detachment process from the upper surface occurs with the increased angle of attack. It results in sudden loss of lift and dangerous stall condition.
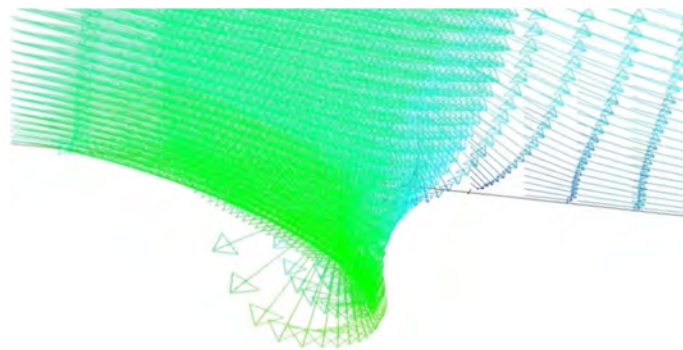
Figure 4.15: Velocity vector with suction at 0.7C position of chord length at 19° angle of attack

Figure 4.15 shows that at higher angle of attack, the separated flow gets reattached and a significant decrease in flow separation is observed while compared to without suction phenomenon on airfoil as shown in Figure 4.14. Because of suction pressure on 0.7C slot, the flow gets reattached as the slot sucks the flow towards the cavity.

4.6   Comparison between Two Different Configurations of Internal Slot

Two different configurations of internal slots are placed individually as passive flow control on the upper surface of the airfoil. Width of slot for two types of internally slotted airfoil is

2% of the chord length of the airfoil. A comparison is made between leading edge chordal slot and tangential internal slot to observe the performance of these two slots on upper surface of airfoil. For avoiding other complexities, performance is observed at fixed 30% chord length slot position on the upper surface of the airfoil. Lift coefficient, drag coefficient and lift to drag ratio are the main parameters for internal slot selection process.
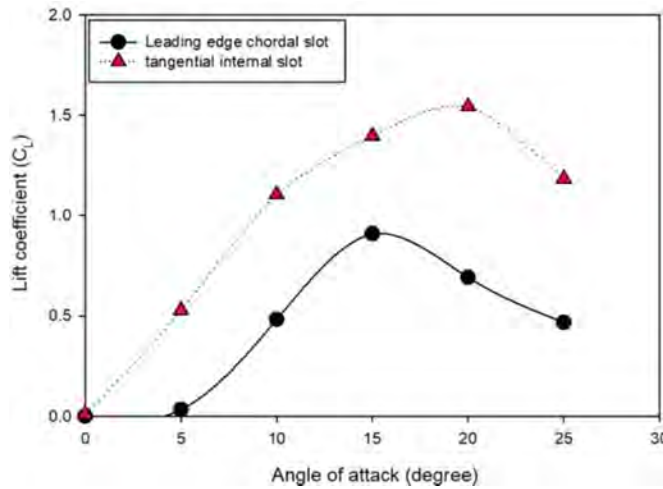
Figure 4.16: Variation of lift coefficient with angle of attack for two configuration of internal slot
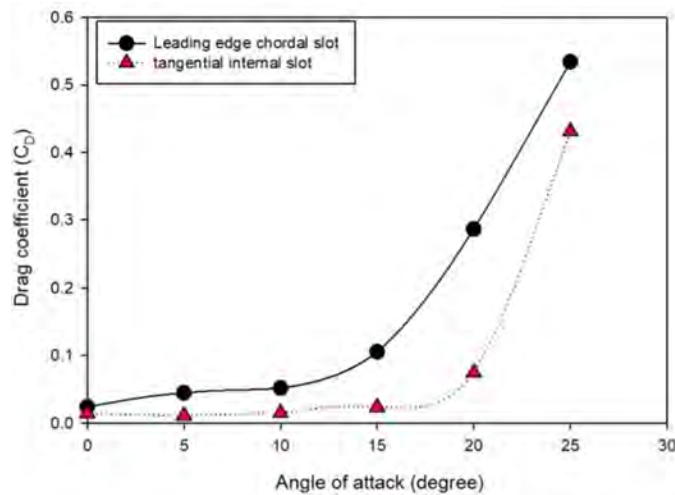
Figure 4.17: Variation of drag coefficient with angle of attack for two configuration of internal slot

The data obtained from Table 7 and 8 are presented in Figure 4.16 and 4.17. The above figures show that the maximum lift coefficient and the minimum drag coefficient can be achieved in case of tangential internal slot than that of leading edge chordal slot. Leading edge chordal slot increases lift coefficient up to 15° angle of attack and after that lift

45

coefficient starts to decrease. Hence, the stall angle occurs at 15° angle of attack in this case whereas the stall angle occurs later with tangential internal slot.
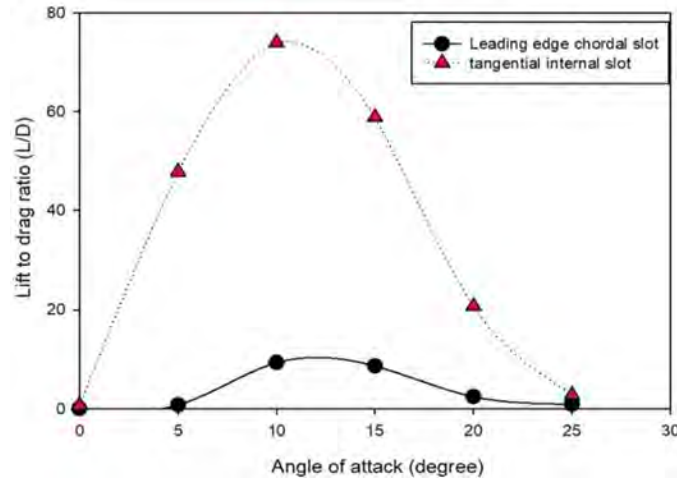
Figure 4.18: Variation of lift to drag ratio with angle of attack for two configuration of internal slot

The data from Table 9 plotted in Figure 4.18 indicates that between these two configurations of internal slots, tangential internal slot enhances the overall lift to drag ratio at different angles of attack in comparison to leading edge chordal slot.
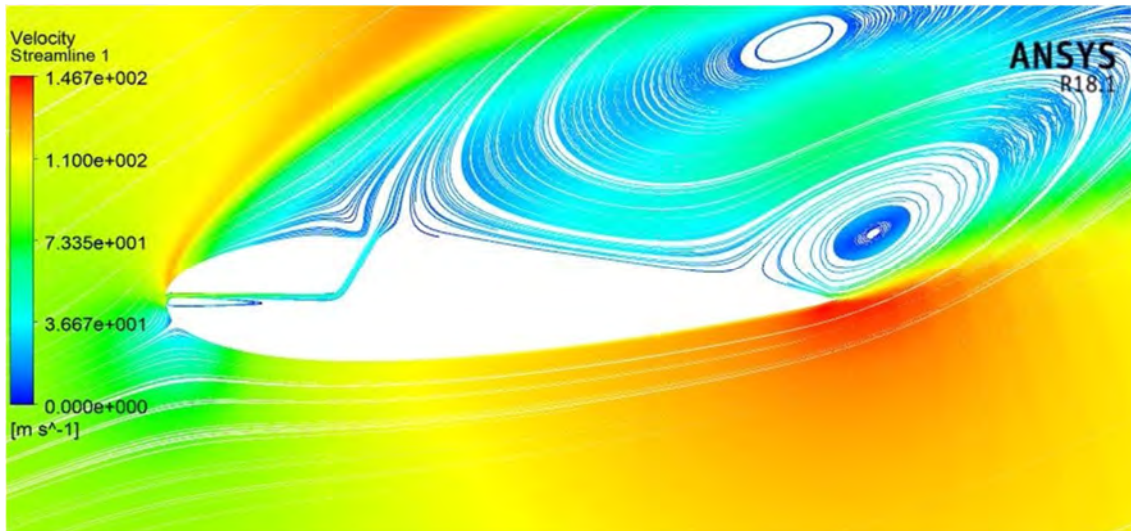
Figure 4.19: Velocity streamline of airfoil with leading edge chordal slot on upper surface at 19° angle of attack

Figure 4.19 shows that at initial leading edge the streamlines loses its energy to stay attached to the surface. From this region the flow is completely separated from the suction side at 19° angle of attack. Here, less fluid flows into the chordal slot and out of the side slot into the

boundary layer due to the movement of the leading edge away from the direction of the flow stream.
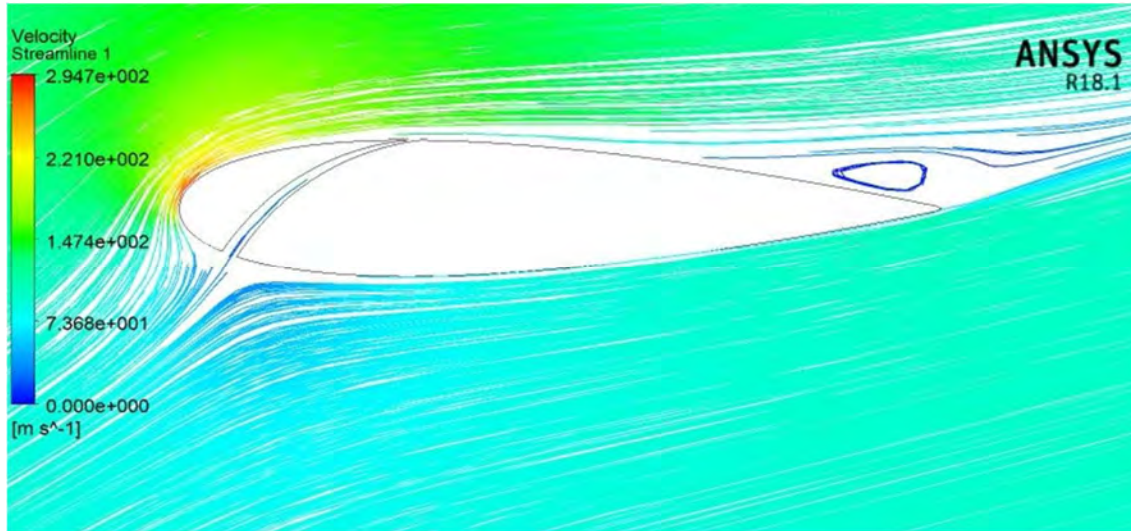
Figure 4.20: Velocity streamline of airfoil with tangential internal slot on upper surface at 19° angle of attack

Figure 4.20 shows that flow detaches near the trailing edge of the upper surface of airfoil. The separation does not occur at the initial stage of chord length rather it occurs far away from the leading edge of airfoil. In this case, tangential internal slot at leading edge of airfoil energizes upper surface of airfoil by allowing high pressurized air from pressure side to suction side and delays flow separation more in comparison to leading edge chordal slot.

4.7   Optimum Slot Location for Tangential Internal Slot

These internal slots are placed at different chord length of airfoil such as 30%, 40%, 50% and 60% chord length slot positions and for avoiding complexities computational runs are made to analyze the best performance at different angles of attack. These slots are acted here as passive flow control mechanism at various conditions.

Figures 4.21 and 4.22 are the graphical representation of Table 10 and 11. They show that among all the slot positions, tangential internal slot at 30% of the chord length increases the lift coefficient and decreases drag coefficient at higher angle of attack. It is known that at higher angle of attack when the air loses too much energy, it separates from the wing causing a decrease in lift. At that moment the air moving across the upper of the wing can be

energized by injecting some of the air from high pressure region to low pressure region through slot to add energy. Here, tangential internal slot at 30% chord length adds energy to the upper surface and stay attached long.
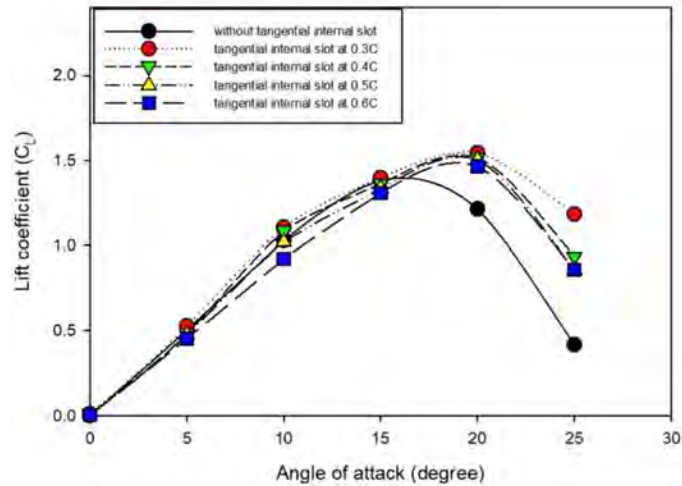
Figure 4.21: Variation of lift coefficient with angle of attack for tangential internal slot
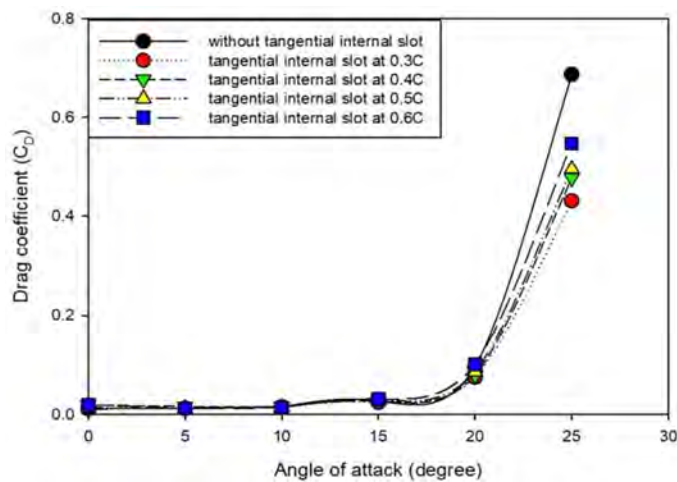
Figure 4.22: Variation of drag coefficient with angle of attack for tangential internal slot

Figure 4.23 is the depiction of Table 12 which shows that 30% chord length slot position is a better position among all the considered tangential internal slot positions. Increased lift force, decreased drag force and a noticeable increment in lift to drag ratio is clearly visible in case of 30% chord length tangential internal slot position.
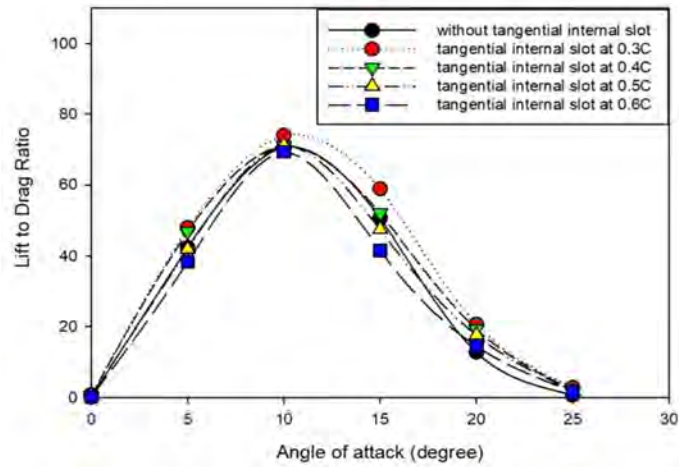
Figure 4.23: Variation of lift to drag ratio with angle of attack for tangential internal slot

4.8 Optimum Condition of Aerodynamic Performance for Airfoil

The following comparison is made among the plain airfoil with and without tangential internal slot and combination of suction at 70% chord length and tangential internal slot at 30% chord length for 15°and 19° angle of attack.
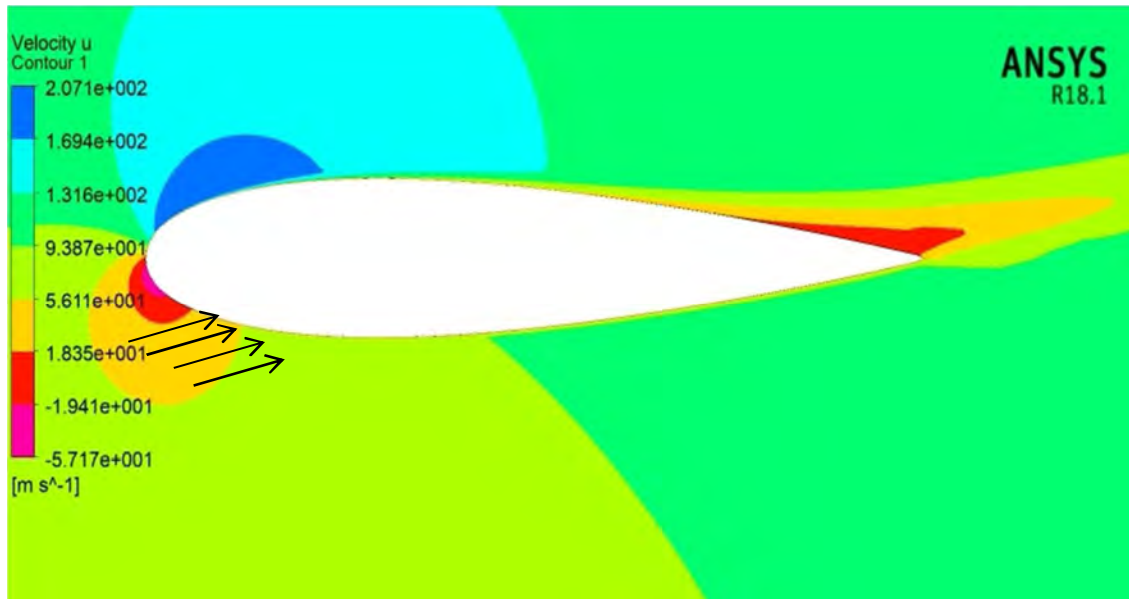
(a) u- velocity contour profile of plain airfoil

The above figure shows that at 15° angle of attack, the presence of negative velocity region starts to be visible. Hence, there is an appearance of flow separation.
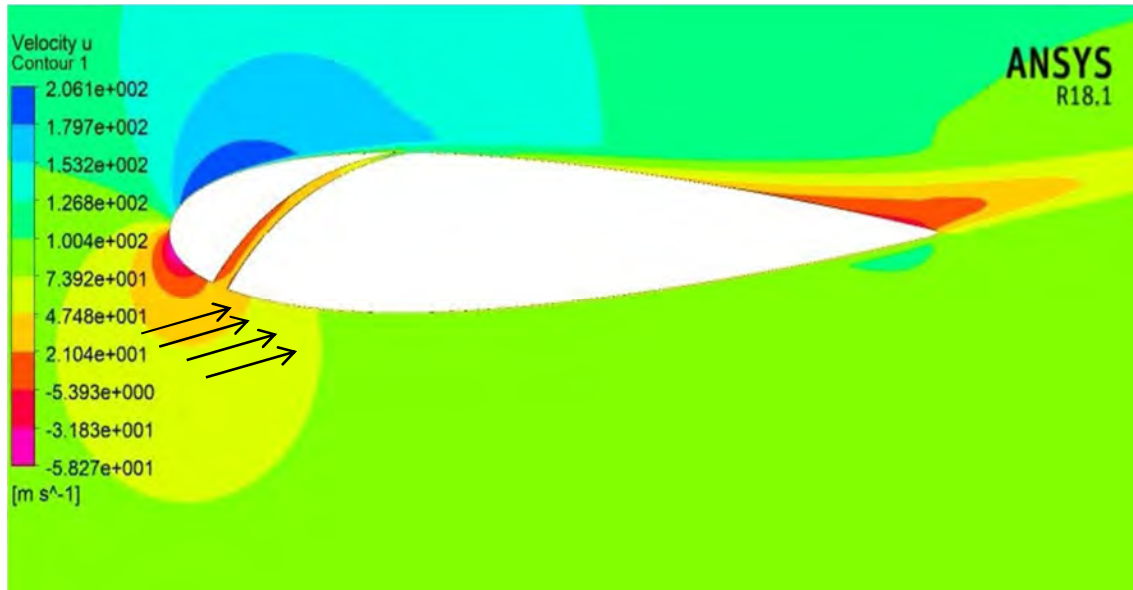
(b) u- velocity contour profile with tangential internal slot

The above figure shows that at 15° angle of attack, the occurrence of negative velocity region is less visible in comparison to plain airfoil.
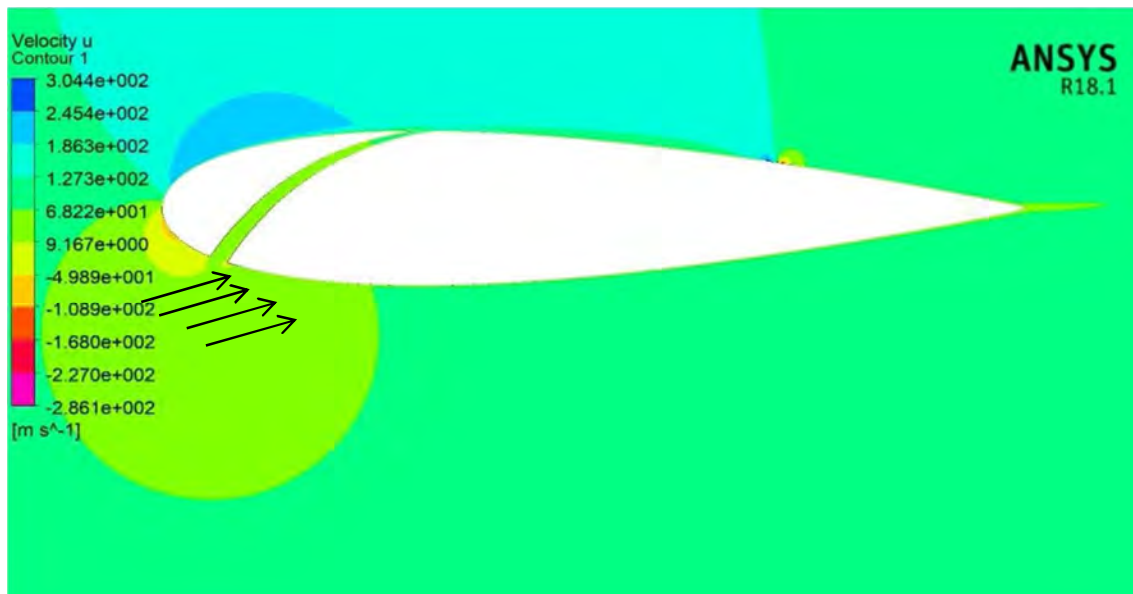
(c) u- velocity contour profile with combined effect of suction and tangential internal slot

Figure 4.24: Comparison of u- velocity contour profile of different configuration of airfoil at 15° angle of attack

Comparing Figure 4.24 (a), (b) and (c), it can be said that at 15° angle of attack the flow separation delays towards the trailing edge with the combined effect of tangential internal slot and suction slot on the upper surface of airfoil. Because of this combination, in Figure 4.24 (c) the presence of negative velocity region is very negligible. Hence, a significant change in flow separation is observed in case of combined effect of tangential internal slot and suction slot on airfoil.
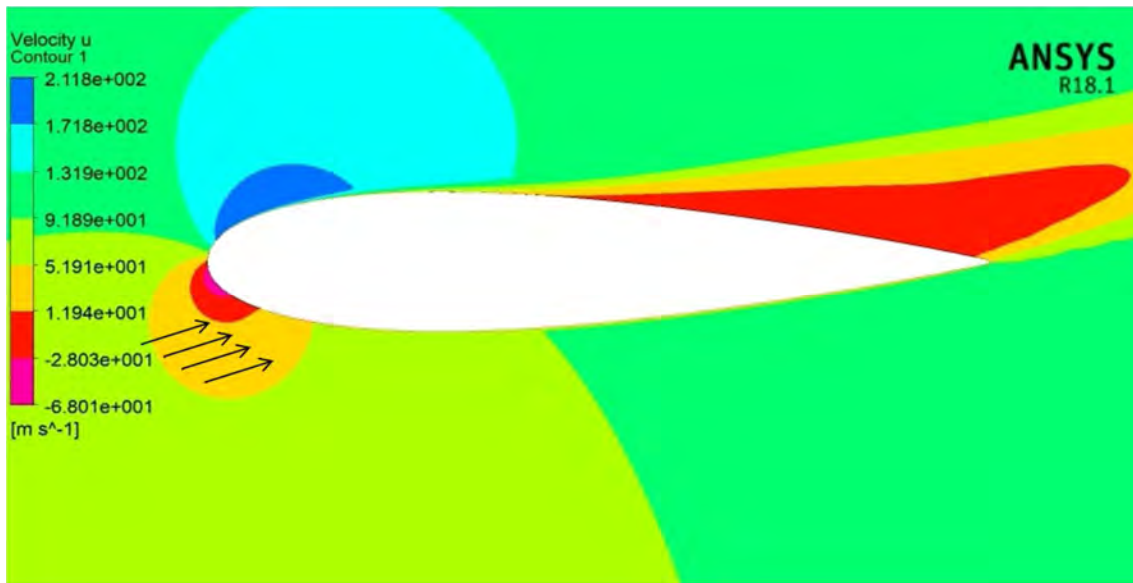
(a) u- velocity contour profile of plain airfoil

The above figure shows that at the very high 19° angle of attack, the presence of negative velocity region is very much visible in comparison to 15° angle of attack as shown in Figure 4.24 (a).

(b) u- velocity contour profile with tangential internal slot

51

The above figure shows that the appearance of negative velocity region is less than that of plain airfoil at 19° angle of attack. Hence, the effect of tangential internal slot energizes the upper surface of airfoil by allowing high pressurized air to go from pressure side to suction side and eventually it delays flow separation more than plain airfoil.
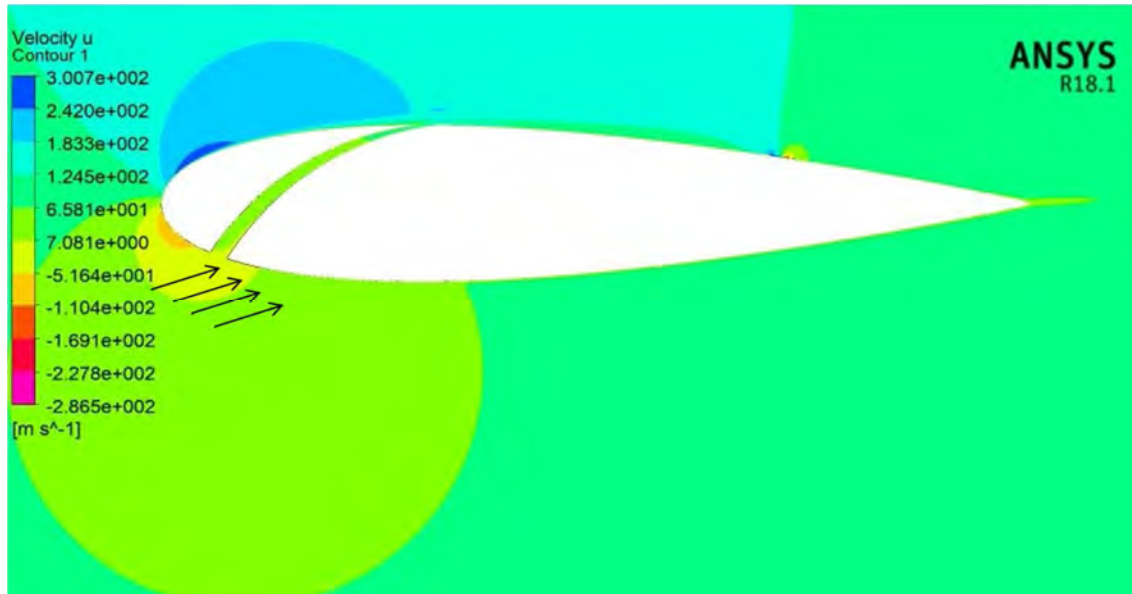
(c) u- velocity contour profile with combined effect of suction and tangential internal slot

Figure 4.25: Comparison of u- velocity contour profile of different configuration of airfoil at 19° angle of attack

Comparing Figure 4.25 (a), (b) and (c), it can be said that the combined effect of tangential internal slot at 0.3C and suction slot at 0.7C with 74% suction pressure on the top surface of airfoil at 19° angle of attack allows air to move from pressure side to suction side tangentially in order to stay attached to upper surface and after that the suction slot near trailing edge sucks the flow into the cavity to cause flow reattachment as well as flow separation delay.

At higher angle of attack, because of internal slot, air can be drawn from the pressure side to suction side tangentially which can add energy to the upper surface and eventually streamline maintain enough energy to stay attached to the wing. After that suction at slot near trailing edge sucks the flow into the cavity to ensure flow reattachment of the detached flow. The combined effect of these two applications results in increased lift coefficient as well as decreased drag coefficient as shown in the above Figure 4.26 and 4.27. These figures are the graphical representation of the Table 13 and 14 which recommend an efficient airfoil design.

In Figure 4.26, there is zero lift at 0° angle of attack for plain airfoil and for tangential internal slot because pressure forces on both sides balance. While considering the combination of suction and tangential internal slot, pressure differential is observed on airfoil because of suction. This pressure differential generates some positive lift greater than zero at 0° angle of attack.
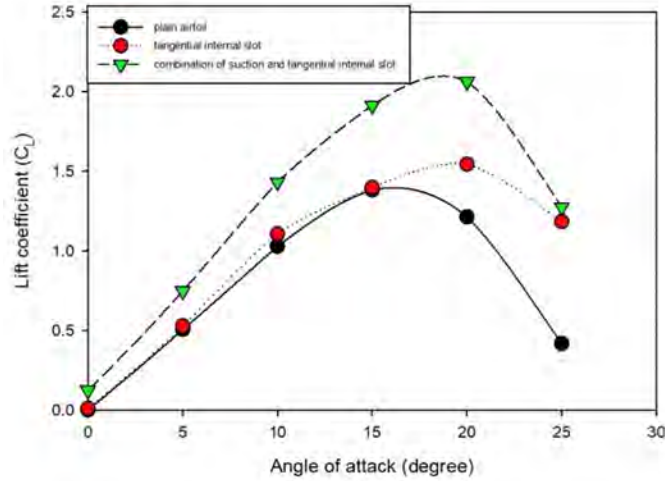
Figure 4.26: Variation of lift coefficient with angle of attack for different configuration of airfoil
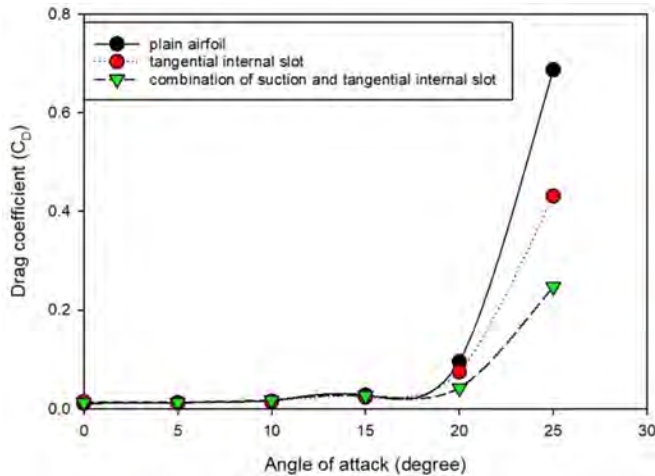
Figure4.27: Variation of drag coefficient with angle of attack for different configuration of airfoil

The data from Table 15 are plotted in Figure 4.28 to show the overall enhancement in lift to drag ratio in case of combined effect on airfoil than that of effect of tangential internal slot on airfoil and plain airfoil. Figure 4.26 shows that after modification the stall occurs just after 19° AOA whereas for plain airfoil the stall occurs at 17° AOA. So the stall is delaying because of combined effect of suction and tangential internal slot on airfoil. For combined effect of suction and tangential internal slot, the maximum lift to drag ratio becomes 17%

whereas for the only effect of tangential internal slot, the ratio becomes 9% than that of plain airfoil.
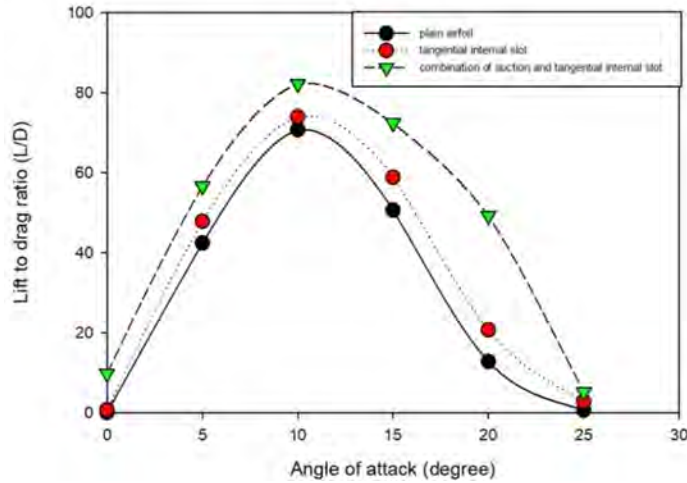
Figure 4.28: Variation of lift to drag ratio with angle of attack for different configuration of airfoil

The location of separation point is another parameter to determine the efficient airfoil design. Having the separation point more near the rear edge of the airfoil is one of the prime concerns in the aspect of flow separation delay. For steady 2D flow, it can be said that the flow is on the verge of separation when the wall shear stress equals to zero [41]. A plot of x-component of wall shear stress of airfoil relative to the chord (x/c) is used to determine the exact flow separation point in both slotted and unslotted cases at 19° AOA. From the flow separation point the wall shear stress becomes negative and causes flow reversal. If the value of wall shear stress is positive, then the flow will not separate or flow will remain attached with the surface.
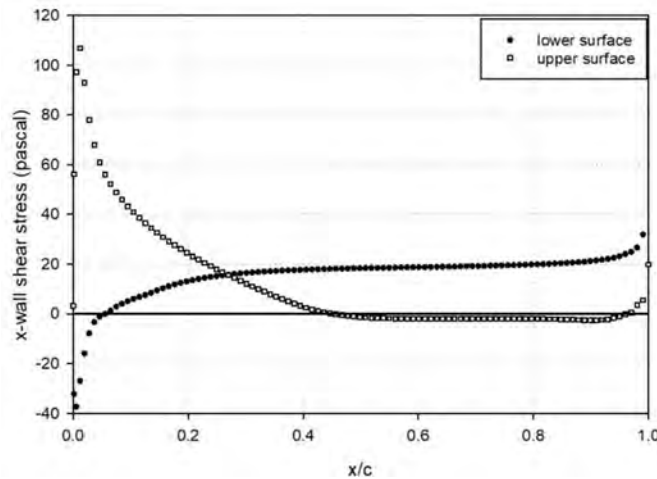
Figure 4.29: x- wall shear stress at different chord length position of plain airfoil at 19° angle of attack

54

Figure 4.29 shows that at 19° angle of attack the wall shear stress becomes negative from 46% of the chord length from leading edge and it becomes positive again at 97% chord length position for plain airfoil. Hence, the separation length is at 51% of the chord length of airfoil for baseline airfoil.
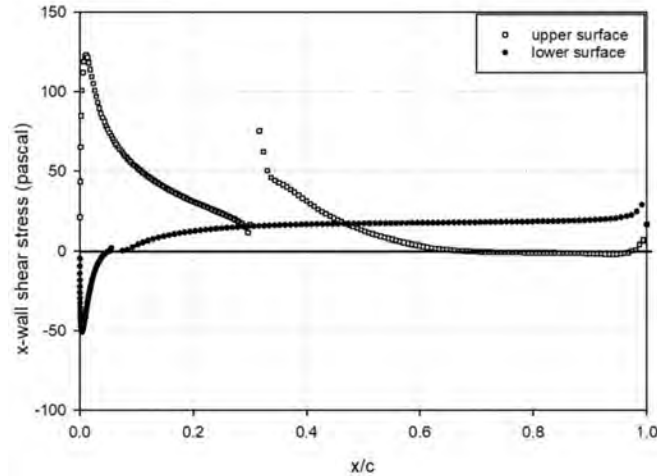
Figure 4.30: x-wall shear stress at different chord length position of airfoil with the effect of tangential internal slot on the upper surface at 19° angle of attack

The above Figure depicts the separation point moves at 68% of the chord length from leading edge of airfoil with effect of 0.3C tangential internal slot on the upper surface of airfoil. Flow reattachment is observed at 97% of chord length position. Therefore, the separation length for this case is 29% of the chord length.
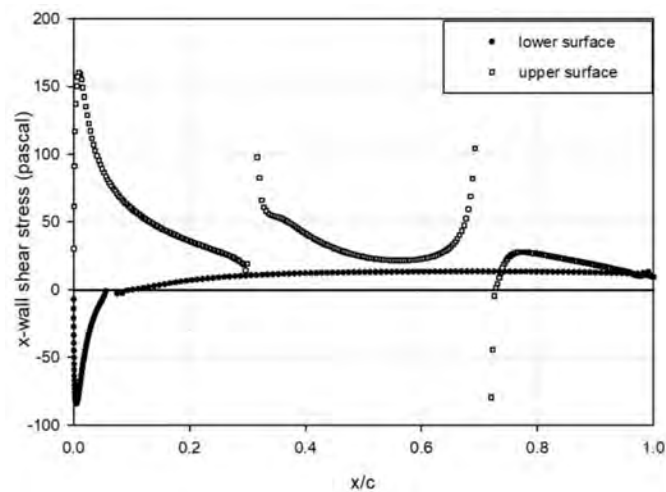
Figure 4.31: x-wall shear stress at different chord length position of airfoil with the combined effect of suction and tangential internal slot on the upper surface at 19° angle of attack

55

Figure 4.31 indicates the separation occurs at 72% of the chord length position from leading edge of airfoil with the combined effect of 30% chord length tangential internal slot position and 70% chord length suction slot on the upper surface of the airfoil. The detached flow immediately reattaches at 73% of chord length position. The modified airfoil with this combined effect creates separation length of 1% of chord length of airfoil.

CONCLUSIONS AND RECOMMENDATIONS

5.1 Conclusions

The main objective of this present study is to enhance the lift to drag ratio of the airfoil by delaying flow separation. In this study, the computational runs are made at 7.12×10^6 Reynolds number. Both active and passive flow control are considered for delay of flow separation. Five suction slot positions and four suction pressures as percentage of atmospheric pressure are studied. Two different configurations of internal slots such as tangential internal slot and leading edge chordal slot are also studied. To observe further improvement, four tangential internal slot positions are then introduced. Lastly, this investigation focuses on both the effect of tangential internal slot near leading edge and suction near trailing edge on airfoil upper surface. The following conclusions can be drawn from the findings of the study:

- Among the considered suction positions along with suction pressure, the slot position at 0.7C with 74% suction pressure results in higher lift force, lower drag force and higher lift to drag ratio at different angle of attack.

- Out of two different configurations of internal slots, tangential internal slot provides better results than that of leading edge chordal slot.

- The maximum lift coefficient and lift to drag ratio as well as the minimum drag coefficient can be achieved for combined effect of tangential internal slot and suction slot. The maximum lift to drag ratio for tangential internal slot becomes 9% while for combination of tangential internal slot and suction the ratio becomes 17% in comparison to plain airfoil.

- In addition, for plain airfoil the stall angle occurs at 17° angle of attack whereas for the combined effect of tangential internal slot and suction it occurs just after 19° angle of attack.

- The effect of tangential internal slot moves the separation point at 68% of the chord length and the combined effect of tangential internal slot and suction moves the separation point at 72% of the chord length while the separation point lies at 46% of the chord length for plain airfoil.

- The flow separation reattaches at 97% of the chord length position for plain airfoil with and without the effect of tangential internal slot and the separation length for plain airfoil is 51% of the chord length while the separation length is 29% of the chord length with the effect of tangential internal slot. The flow reattachment is observed at 73% of the chord length position for the combined effect of suction and tangential internal slot and the separation length is 1% of the chord length for this case.

5.2   Recommendations

Aerodynamic characteristics for the considered airfoil have been presented in this study. Combination of tangential internal slot and suction pressure is applied to enhance aerodynamic characteristics specifically to improve the lift to drag ratio. Since airfoil plays significant role to improve aerodynamic performance, further study can be done regarding active and passive flow control system. However, the following recommendations can be made for future work related to present study:

- The study on airfoil along with all the modifications can be conducted considering higher Reynolds number

- Further investigations can be done for different slot geometry with other passive flow control mechanism on the airfoil.

- Other turbulence model can be used to compare the result with that of present study.

- Different angle of suction pressure can be used for possible improvement of the result.

REFERENCES

[1]   Padfield, G. D., and Lawrence, B. A., "The birth of flight control: An engineering analysis of the Wright brothers' 1902 glider", *The Aeronautical Journal*, Vol. 107, pp. 697-718, 2003.

[2]   Huang, L., Huang, P. G., LeBeau, R. P., and Hauser, T., "Numerical Study of Blowing and Suction Control Mechanism on NACA 0012 Airfoil", *Journal of Aircraft*, Vol 41: 5, pp. 1005–1013, 2014.

[3]   Vrchota, P., Prachar, A., Peng, S.-H., Tormalm, M., and Eliasson, P., "Numerical studies of active flow control on wing tip extension", *Aircraft Engineering and Aerospace Technology*, Vol. 91(2), pp. 346-352, 2018.

[4]   Zalovick, J. A., Wetmore, J. W., and Von doenhoff, A., E., L., "Flight Investigation of Boundary-layer by Suction Slots on an NACA 35-215 Low-drag Airfoil at High Reynolds Numbers", NACA Advance Confidential Report No. 4B29, pp.1- 16, 1944.

[5]   Müller-Vah, H. F., Strangfeld, C., Nayeri, C. N., Paschereit, C. O., and Greenblatt, D.," Control of Thick Airfoil, Deep Dynamic Stall Using Steady Blowing", *AIAA Journal*, Vol 53 (2), pp. 277-295, 2015.

[6]   Chen, C., and Wygnanski, I., "Flow Control on a Thick Airfoil Using Suction Compared to Blowing", *AIAA Journal*, Vol 51 (6), pp. 1462-1472, 2013.

[7]   Radespiel, R., Burnazzi, M., Casper, M., and Scholz, P., "Active flow control for high lift with steady blowing", *The Aeronautical Journal*, Vol 120, Issue 1223, pp. 171-200, 2016.

[8]   Yousefi, K., Saleh, R., and Zahedi, P., "Numerical study of blowing and suction slot geometry optimization on NACA 0012 airfoil", *Journal of Mechanical Science and Technology*, Vol 28 (4), pp. 1297-1310, 2014.

[9] Zhu, H., Hao, W., Li. C., Ding, Q., and Wu, B., "Application of flow control strategy of blowing, synthetic and plasma jet actuators in vertical axis wind turbines", Aerospace Science and Technology, Vol 88, pp. 468-480.

[10] Liu, P. Q., Duan, H. S., Chen, J. Z., and He, Y. W., "Numerical study of suction-blowing flow control technology for an airfoil", *Journal of aircraft*, Vol 47(1), pp. 229-239, 2010.

[11] Narsipur, S., Hosangadi, P., Gopalarathnam, A., and Edwards, J. R., "Variation of Leading-Edge Suction at Stall for Steady and Unsteady Airfoil Motions", *54th AIAA Aerospace Sciences Meeting*, pp. 1-18, 2016.

[12] Ibrahim, A., and Filippone, A., "Supersonic aerodynamics of a projectile with slot cavities", *The Aeronautical Journal*, Vol. 114 (1151), pp. 15-24, 2010.

[13] Arunraj, R., Logesh, K., Balaji, V., Ravichandran, T., and Yuvashree, G. K., "Experimental Investigation of Lift Enhancement by Suction-assisted Delayed Separation of the Boundary Layer on NACA 0012 Airfoil", *International Journal of Abient Energy*, Vol 140, pp. 243-247, 2017.

[14] Azim, R., Hasan, M. M., and Ali, M., "Numerical Investigation on the Delay of Boundary Layer Separation by Suction for NACA 4412", *6th BSME International Conference on Thermal Engineering (ICTE 2014)*, Procedia Engineering, Vol 105, pp. 329-334, 2015.

[15] Zhang, J., Xu, K., Yang, Y., Yan, R., Patel, P., and Zha, G., "Aircraft Control Surfaces Using Co-flow Jet Active Flow Control Airfoil", *36th AIAA Applied Aerodynamics Conference 2018*, Vol 2, pp. 812-840, 2018.

[16] Petz, R., and Nitsche, W., "Active Separation Control on the Flap of a Two-Dimensional Generic High-Lift Configuration", *Journal of aircraft,* Vol 44, No 3, pp. 865-874, 2007.

[17]   Gardarin, B., Jacquin, L., and Geffroy, P., "Flow Separation Control With Vortex Generator," *AIAA Paper 2008-3773*, pp. 1-8, 2008.

[18]   Serakawi, A. R., and Ahmad., K. A., "Experimental Study of Half-Delta Wing Vortex Generator for Flow Separation Control", *Journal of aircraft*, Vol 49, No 1, pp. 76-81, 2012.

[19]   Seshagiri, A., Cooper, E., and Traub, L. W., "Effects of Vortex Generators on an Airfoil at Low Reynolds Numbers", *Journal of aircraft*, Vol 46, No 1, pp. 116-122, 2009.

[20]   Luo, D., Huang, D., and Sun, X., "Passive flow control of a stalled airfoil using a microcylinder", *Journal of Wind Engineering & Industrial Aerodynamic,* Vol 170, pp. 256-273, 2017.

[21]   Johari, H., Henoch, C., Custodio, D., and Levshin, A., "Effects of Leading-Edge Protuberances on Airfoil Performance", *AIAA Journal*, Vol 45, No 11, pp. 2634-2642, 2007.

[22]   Joo, W., Lee, B., Yee, K., and Lee, D., "Combining Passive Control Method for Dynamic Stall Control", *Journal of aircraft*, Vol 43, No 4, pp. 1120-1128, 2006.

[23]   Lawson, S. J., and Barakos, G. N., "Assessment of Passive Flow Control for Transonic Cavity Flow Using Detached-Eddy Simulation", *Journal of aircraft*, Vol 46, No 3, pp. 1009-1029, 2009.

[24]   Chauhan, M. K., Dutta, S., More, B. S., and Gandhi, B. K., "Experimental investigation of flow over a square cylinder with an attached splitter plate at intermediate Reynolds number", *Journal of Fluids and Structures,* Vol 76, pp. 319-335, 2018.

[25]   Kolzsch, A., and Breitsamter, C., "Vortex-Flow Manipulation on a Generic Delta-Wing Configuration", *Journal of aircraft*, Vol 51, No 5, pp. 1380-1390, 2014.

[26]   Obiga, O., "Investigation of the Performance of a Slotted Aerofoil at Low Reynolds Numbers", Doctor of Philosophy, Department of Mechanical, Materials and Manufacturing Engineering, The University of Nottingham, 2016.

[27]   Moshfeghi, M., Shams, S., and Hur, N., "Aerodynamic performance enhancement analysis of horizontal axis wind turbines using a passive flow control method via split blade", *Journal of Wind Engineering and Industrial Aerodynamics*, Vol 167, pp. 148–159, 2017.

[28]   Belamadi, R., Djemili, A., Ilinca, A., and Mdouki, R., "Aerodynamic performance analysis of slotted airfoils for application to wind turbine blades", *Journal of Wind Engineering and Industrial Aerodynamics*, Vol 151, pp. 79–99, 2016.

[29]   Ni, Z., Dhanak, M., and Su, T., "Improved Performance of a Slotted Blade Using a Novel Slot Design", *Journal of Wind Engineering & Industrial Aerodynamics*, Vol 189, pp. 34-44, 2019.

[30]   Ni, Z., Dhanak, M., and Su, T., "Performance Characteristics of Airfoils with Leading-Edge Tubercles and an Internal Slot", *AIAA Journal*, Vol 57 (1), pp. 1-14, 2019.

[31]   Houghton, E. L., and Carpenter, P. W., "Aerodynamics for Engineering Students", Butterworth-Heinemann, 5th Edition, 2003.

[32]   Pilot's Handbook of Aeronautical Knowledge, U.S. Department of Transportation, FEDERAL AVIATION ADMINISTRATION, Flight Standards Service, 2016.

[33]   McCarty, M., "The Measurement of the Pressure Distribution over the Wing of an Aircraft in Flight", M.Sc. Thesis, School of Aerospace, Civil and Mechanical Engineering, University of New South Wales, Australia, 2008.

[34]   Groh, R., "Boundary Layer Separation over the Top Surface of a Wing", Aerospace Engineering Blog, 2016.

[35]   Abbott, I. H., and Doenhoff, A. E. V., "Theory of Wing Sections Including a Summary of Aerofoil Data", Dover Publications, New York, 1990.

[36]   Ramesh, P., "Numerical and Experimental investigation of the effect of geometry modification on the Aerodynamic characteristics of a NACA 64 (2)-415 wing", M.Sc. Thesis, Royal Institute of Technology, Stockholm, Sweden, 2013.

[37]   Spalart, P. R., and Allmaras, S. R., "A ONE-EQUATION TURBULENCE MODEL FOR AERODYNAMIC FLOWS", *AIAA-92-G439*, pp. 1-22, 1992.

[38]   "ANSYS FLUENT 12.0 User's Guide", 2012.

[39]   Timmer, W. A., "Two-dimensional low-Reynolds number wind tunnel results for airfoil NACA 0018", *Wind Engineering*, Vol 32, pp. 525–537, 2009.

[40]   Anderson, J. D., "Introduction to Flight", McGraw Hill, 3rd Edition, 1989.

[41]   Cebeci, T., Mosinskis, G. J., and Smith, A. M. O., "Calculation of separation points in incompressible turbulent flows", *Journal of Aircraft*, Vol 9 (9), pp. 618–624, 1972.

Table 3: Calculated Values of Lift to Drag Ratio of Airfoil without slot and with slot at 0.6C, 0.7C and 0.8C Slot Position with 74% Suction Pressure at Different Angles of Attack				
AOA	Lift to Drag ratio			
	Without suction slot	0.6C suction slot	0.7C suction slot	0.8C suction slot
0°	0.000245	34.4451	41.16309331	14.62791
5°	42.39156	74.6934	82.38773864	70.83997
10°	70.73271	76.3695	82.69348638	72.76122
15°	50.62768	64.5271	71.99571927	58.42647
20°	12.77718	38.5932	44.81260785	32.94316
25°	0.607782	1.3264	2.831563506	3.237688

Table 4: Calculated Values of Lift Coefficient of Airfoil at 0.7C Slot Position with Different Suction Pressure at Different Angles of Attack					
AOA	Lift coefficient				
	without suction pressure	44% suction pressure	54% suction pressure	64% suction pressure	74% suction pressure
0°	0.00	0.25	0.28	0.31	0.33848
5°	0.50624	0.8114	0.8435	0.87	0.9192
10°	1.0281	1.377	1.37	1.443	1.4841
15°	1.3833	1.93	2.0114	2.05	2.0855
20°	1.2141	2.38	2.42	2.44	2.6925
25°	0.41771	0.68	0.69	0.72	0.88795

Table 5: Calculated Values of Drag Coefficient of Airfoil at 0.7C Slot Position with Different Suction Pressure at Different Angles of Attack					
AOA	Drag coefficient				
	without suction pressure	44% suction pressure	55% suction pressure	64% suction pressure	74% suction pressure
0°	0.010678	0.0099	0.0097	0.009	0.008223
5°	0.011942	0.0139	0.0135	0.0117	0.011157
10°	0.014535	0.0193	0.0188	0.0185	0.017947
15°	0.027323	0.03345	0.03101	0.0298	0.028967
20°	0.095021	0.0787	0.063	0.06	0.060084
25°	0.68727	0.38	0.34	0.31	0.31353

Table 6: Calculated Values of Lift to Drag Ratio of Airfoil at 0.7C Slot Position with Different Suction Pressure at Different Angles of Attack

AOA	Lift to drag Ratio				
	without suction pressure	44% suction pressure	54% suction pressure	64% suction pressure	74% suction pressure
0°	0.00024480240	25.25	28.87	34.44	41.1631
5°	42.3915592	58.37	62.48	74.36	82.38774
10°	70.7327141	71.35	72.87	78	82.69349
15°	50.6276763	57.69	64.86	68.79	71.99572
20°	12.7771756	30.24	38.41	40.67	44.81261
25°	0.607781512	1.79	2.02	2.32	2.832105

Table 7: Calculated Values of Coefficient of Lift of Airfoil at 0.3C Slot Position at Different Angles of Attack

AOA	Lift Coefficient	
	Leading edge chordal slot	Tangential internal slot
0°	0.00001	0.01
5°	0.03299	0.52841
10°	0.482306	1.10584
15°	0.91001	1.39811
20°	0.69199	1.5444
25°	0.46742	1.1842

Table 8: Calculated Values of Coefficient of Drag of Airfoil at 0.3C Slot Position at Different Angles of Attack

AOA	Drag Coefficient	
	Leading edge chordal slot	Tangential internal slot
0°	0.023639	0.014398
5°	0.044426	0.011044
10°	0.051676	0.014943
15°	0.1053	0.023749
20°	0.28647	0.074572
25°	0.53426	0.43123

Table 9: Calculated Values of Lift to Drag Ratio of Airfoil at 0.3C Slot Position at Different Angles of Attack		
AOA	**Lift to Drag Ratio**	
	Leading edge chordal slot	**Tangential internal slot**
0°	0.00042303	0.694540908
5°	0.742583172	47.84588917
10°	9.333268829	74.00388142
15°	8.642070275	58.87026822
20°	2.415575802	20.71018613
25°	0.874892374	2.74609837

Table 10: Calculated Values of Lift Coefficient of Airfoil with the Effect of Tangential Internal Slot at Different Position of Chord Length at Different Angles of Attack					
AOA	**Lift Coefficient**				
	Without tangential internal slot	**0.3C tangential internal slot**	**0.4C tangential internal slot**	**0.5C tangential internal slot**	**0.6C tangential internal slot**
0°	0.000002614	0.01	0.009	0.007	0.003
5°	0.50624	0.52841	0.48399	0.47845	0.45365
10°	1.0281	1.10584	1.08371	1.01917	0.92197
15°	1.3833	1.39811	1.364	1.3346	1.3084
20°	1.2141	1.5444	1.5175	1.5043	1.4658
25°	0.41771	1.1842	0.93605	0.85636	0.85922

Table 11: Calculated Values of Drag Coefficient of Airfoil with the Effect of Tangential Internal Slot at Different Position of Chord Length at Different Angles of Attack					
AOA	**Drag Coefficient**				
	Without tangential internal slot	**0.3C tangential internal slot**	**0.4C tangential internal slot**	**0.5C tangential internal slot**	**0.6C tangential internal slot**
0°	0.010678	0.014398	0.018393	0.013019	0.018771
5°	0.011942	0.011044	0.015189	0.011418	0.011830
10°	0.014535	0.014943	0.015230	0.014322	0.013298
15°	0.027323	0.023749	0.026213	0.028189	0.030762
20°	0.095021	0.074572	0.078553	0.085265	0.100711
25°	0.68727	0.431230	0.477606	0.495542	0.547510

Table 12: Calculated Values of Lift to Drag Ratio of Airfoil with the Effect of Tangential Internal Slot at Different Position of Chord Length at Different Angles of Attack

AOA	Lift to Drag Ratio				
	Without tangential internal slot	0.3C tangential internal slot	0.4C tangential internal slot	0.5C tangential internal slot	0.6C tangential internal slot
0°	0.000245	0.69454091	0.489316588	0.537676	0.159821
5°	42.39156	47.8458892	46.86646654	41.90314	38.34742
10°	70.73271	74.0038814	71.15594222	71.16115	69.33148
15°	50.62768	58.8702682	52.03524969	47.34443	41.55777
20°	12.77718	20.7101861	19.31812561	17.64272	14.55446
25°	0.607782	2.74609837	1.959879063	1.728127	1.569322

Table 13: Calculated Values of Lift Coefficient of Plain Airfoil, Effect of 0.3C Tangential Internal Slot and Combined Effect of 0.3C Tangential Internal Slot and 0.7c Suction Slot with 74% Suction Pressure on Airfoil at Different Angles of Attack

AOA	Lift Coefficient		
	Plain airfoil	Effect of tangential internal slot	Combined effect of tangential internal slot and suction Slot
0°	0.000002614	0.01	0.12315
5°	0.50624	0.52841	0.748112
10°	1.0281	1.10584	1.4334
15°	1.3833	1.39811	1.9145
20°	1.2141	1.5444	2.0635
25°	0.41771	1.1842	1.2764

Table 14: Calculated Values of Drag Coefficient of Plain Airfoil, Effect of 0.3C Tangential Internal Slot and Combined Effect of 0.3C Tangential Internal Slot and 0.7C Suction Slot with 74% Suction Pressure on Airfoil at Different Angles of Attack

AOA	Drag Coefficient		
	Plain airfoil	Effect of tangential internal slot	Combined effect of tangential internal slot and suction slot
0°	0.010678	0.014398	0.012593
5°	0.011942	0.011044	0.013214
10°	0.014535	0.014943	0.01743
15°	0.027323	0.023749	0.026442
20°	0.095021	0.074572	0.041886
25°	0.68727	0.43123	0.24712

Table 15: Calculated Values of Lift to Drag Ratio of Plain Airfoil, Effect of 0.3C Tangential Internal Slot and Combined Effect of 0.3C Tangential Internal Slot and 0.7C Suction Slot with 74% Suction Pressure on Airfoil at Different Angles of Attack

AOA	Lift to Drag Ratio		
	Plain airfoil	Effect of tangential internal slot	Combined effect of tangential internal slot and suction slot
0°	0.000244802	0.694540908	9.77924
5°	42.3915592	47.8459	56.61511
10°	70.73271414	74.0039	82.23752
15°	50.62767632	58.8703	72.40375
20°	12.77717557	20.7102	49.26467
25°	0.607781512	2.74609837	5.16510

Table 16: Parameters Used in Calculation

Run no.	AOA	Suction Slot Position	Suction Pressure	Leading Edge Chordal Slot position	Tangential Internal Slot position
Run 1	0°	-	-	-	-
Run 2	5°	-	-	-	-
Run 3	10°	-	-	-	-
Run 4	15°	-	-	-	-
Run 5	16°	-	-	-	-
Run 6	17°	-	-	-	-
Run 7	18°	-	-	-	-
Run 8	19°	-	-	-	-
Run 9	20°	-	-	-	-
Run 10	25°	-	-	-	-
Run 11	0°	0.6C	74%	-	-
Run 12	5°	0.6C	74%	-	-
Run 13	10°	0.6C	74%	-	-
Run 14	15°	0.6C	74%	-	-
Run 15	20°	0.6C	74%	-	-
Run 16	25°	0.6C	74%	-	-
Run 17	0°	0.7C	44%	-	-
Run 18	5°	0.7C	44%	-	-
Run 19	10°	0.7C	44%	-	-
Run 20	15°	0.7C	44%	-	-
Run 21	20°	0.7C	44%	-	-
Run 22	25°	0.7C	44%	-	-
Run 23	0°	0.7C	54%	-	-
Run 24	5°	0.7C	54%	-	-

		Table 16: Parameters Used in Calculation			
Run no.	**AOA**	**Suction Slot Position**	**Suction Pressure**	**Leading Edge Chordal Slot position**	**Tangential Internal Slot position**
Run 25	10°	0.7C	54%	-	-
Run 26	15°	0.7C	54%	-	-
Run 27	20°	0.7C	54%	-	-
Run 28	25°	0.7C	54%	-	-
Run 29	0°	0.7C	64%	-	-
Run 30	5°	0.7C	64%	-	-
Run 31	10°	0.7C	64%	-	-
Run 32	15°	0.7C	64%	-	-
Run 33	20°	0.7C	64%	-	-
Run 34	25°	0.7C	64%	-	-
Run 35	0°	0.7C	74%	-	-
Run 36	5°	0.7C	74%	-	-
Run 37	10°	0.7C	74%	-	-
Run 38	15°	0.7C	74%	-	-
Run 39	20°	0.7C	74%	-	-
Run 40	25°	0.7C	74%	-	-
Run 41	0°	0.8C	74%	-	-
Run 42	5°	0.8C	74%	-	-
Run 43	10°	0.8C	74%	-	-
Run 44	15°	0.8C	74%	-	-
Run 45	20°	0.8C	74%	-	-
Run 46	25°	0.8C	74%	-	-
Run 47	0°	-	-	0.3C	-
Run 48	5°	-	-	0.3C	-
Run 49	10°	-	-	0.3C	-
Run 50	15°	-	-	0.3C	-
Run 51	20°	-	-	0.3C	-
Run 52	25°	-	-	0.3C	-
Run 53	0°	-	-	-	0.3C
Run 54	5°	-	-	-	0.3C
Run 55	10°	-	-	-	0.3C
Run 56	15°	-	-	-	0.3C
Run 57	19°	-	-	-	0.3C
Run 58	20°	-	-	-	0.3C
Run 59	25°	-	-	-	0.3C
Run 60	0°	-	-	-	0.4C
Run 61	5°	-	-	-	0.4C

Table 16: Parameters Used in Calculation					
Run no.	AOA	Suction Slot Position	Suction Pressure	Leading Edge Chordal Slot position	Tangential Internal Slot position
Run 62	10°	-	-	-	0.4C
Run 63	15°	-	-	-	0.4C
Run 64	20°	-	-	-	0.4C
Run 65	25°	-	-	-	0.4C
Run 66	0°	-	-	-	0.5C
Run 67	5°	-	-	-	0.5C
Run 68	10°	-	-	-	0.5C
Run 69	15°	-	-	-	0.5C
Run 70	20°	-	-	-	0.5C
Run 71	25°	-	-	-	0.5C
Run 72	0°	-	-	-	0.6C
Run 73	5°	-	-	-	0.6C
Run 74	10°	-	-	-	0.6C
Run 75	15°	-	-	-	0.6C
Run 76	20°	-	-	-	0.6C
Run 77	25°	-	-	-	0.6C
Run 78	0°	0.7C	74%	-	0.3C
Run 79	5°	0.7C	74%	-	0.3C
Run 80	10°	0.7C	74%	-	0.3C
Run 81	15°	0.7C	74%	-	0.3C
Run 82	19°	0.7C	74%	-	0.3C
Run 83	20°	0.7C	74%	-	0.3C
Run 84	25°	0.7C	74%	-	0.3C